Monthly Notices of the ROYAL ASTRONOMICAL SOCIETY

MNRAS **507,** 74–89 (2021)
Advance Access publication 2021 July 19

https://doi.org/10.1093/mnras/stab2058

AGNIFS survey of local AGN: GMOS-IFU data and outflows in 30 sources

D. Ruschel-Dutra,[1★] T. Storchi-Bergmann,[2] A. Schnorr-Müller,[2] R. A. Riffel,[3] B. Dall'Agnol de Oliveira,[2] D. Lena,[4,5,6] A. Robinson,[7] N. Nagar[8] and M. Elvis[9]

[1]*Departamento de Física, Universidade Federal de Santa Catarina, P.O. Box 476, 88040-900 Florianópolis, SC, Brazil*
[2]*Departamento de Astronomia, Universidade Federal do Rio Grande do Sul, IF, CP 15051, 91501-970 Porto Alegre, RS, Brazil*
[3]*Departamento de Física, Centro de Ciências Naturais e Exatas, Universidade Federal de Santa Maria, 97105-900 Santa Maria, RS, Brazil*
[4]*SRON Netherlands Institute for Space Research, Sorbonnelaan 2, NL-3584 CA Utrecht, the Netherlands*
[5]*Department of Astrophysics/IMAPP, Radboud University Nijmegen, PO Box 9010, NL-6500 GL Nijmegen, the Netherlands*
[6]*ASML Netherlands B.V., De Run 6501, NL-5504 DR Veldhoven, the Netherlands*
[7]*School of Physics and Astronomy, Rochester Institute of Technology, 85 Lomb Memorial Dr., Rochester, NY 14623, USA*
[8]*Departamento de Astronomía, Universidad de Concepción, Casilla 160-C, Concepción, Chile*
[9]*Harvard-Smithsonian Center for Astrophysics, 60 Garden Street, Cambridge, MA 02138, USA*

Accepted 2021 July 1. Received 2021 May 31; in original form 2020 September 8

ABSTRACT

We analyse optical data cubes of the inner kiloparsec of 30 local ($z \leq 0.02$) active galactic nucleus (AGN) hosts that our research group, AGNIFS, has collected over the past decade via observations with the integral field units of the Gemini Multi-Object Spectrographs. Spatial resolutions range between 50 and 300 pc and spectral coverage is from 4800 or 5600 to 7000 Å, at velocity resolutions of $\approx$50 km s^{-1}. We derive maps of the gas excitation and kinematics, and determine the AGN ionization axis – which has random orientation relative to the galaxy – and the kinematic major axes of the emitting gas. We find that rotation dominates the gas kinematics in most cases, but is disturbed by the presence of inflows and outflows. Outflows have been found in 21 nuclei, usually along the ionization axis. The gas velocity dispersion is traced by W_{80} (velocity width encompassing 80 per cent of the line flux), adopted as a tracer of outflows. In seven sources, W_{80} is enhanced perpendicularly to the ionization axis, indicating lateral expansion of the outflow. We have estimated mass-outflow rates $\dot{M}$ and powers $\dot{E}$, finding median values of $\log[\dot{M}/(\mathrm{M}_\odot\,\mathrm{yr}^{-1})] = -2.1^{+1.6}_{-1.0}$ and $\log[\dot{E}/(\mathrm{erg\,s}^{-1})] = 38.5^{+1.8}_{-0.9}$, respectively. Both quantities show a mild correlation with the AGN luminosity (L_{AGN}). $\dot{E}$ is of the order of 0.01 L_{AGN} for four sources, but much lower for the majority (nine) of the sources, with a median value of $\log[\dot{E}/L_{\mathrm{AGN}}] = -5.34^{+3.2}_{-0.9}$, indicating that typical outflows in the local Universe are unlikely to significantly impact their host galaxy evolution.

Key words: galaxies: active – galaxies: kinematics and dynamics – galaxies: nuclei – galaxies: Seyfert.

1 INTRODUCTION

The discovery of correlations between the mass of the central supermassive black hole (SMBH) and various properties of the host galaxy, such as the host spheroid mass and stellar velocity dispersion (Ferrarese & Merritt 2000; Gebhardt et al. 2000; Gültekin et al. 2009; Kormendy & Ho 2013; van den Bosch 2016), or the similar evolution of the cosmic star formation rate (SFR) density and the black hole accretion rate density (Madau & Dickinson 2014) points to the growth of SMBHs being closely linked to the stellar mass assembly of their host galaxies. It is believed that this link emerges due to both the mass transfer to the inner region of the galaxy that also feeds the SMBH (Storchi-Bergmann & Schnorr-Müller 2019) and the regulating effect of feedback from the triggered active galactic nuclei (AGNs) on the star formation in the host galaxy (Harrison 2017). The role of AGN feedback is supported by cosmological simulations and models of galaxy evolution (Springel, Di Matteo & Hernquist 2005; Vogelsberger et al. 2014; Schaye et al. 2015): feedback is required to reproduce observables such as the shape of the galaxy luminosity function, the colour bimodality of the galaxy population in the local Universe, and the low star formation efficiency in the most massive galaxies (Alexander & Hickox 2012; Fabian 2012; Harrison 2017).

AGN feedback consists of the injection of mechanical energy (through radio jets) and/or radiative energy (through accretion radiation coupling to the gas on small scales and launching outflows) on the host interstellar and circumgalactic medium by the AGN. These two modes of energy injection are referred to as mechanical and radiative AGN feedback, respectively. Examples of mechanical AGN feedback in action have been found in dense environments in the local Universe, i.e. in the surroundings of elliptical galaxies in the centres of galaxy groups and clusters, where radio jets driven by low-luminosity AGN activity heat the circumgalactic medium through the injection of mechanical energy, reducing the cooling rate of the hot gas and maintaining star formation in the central galaxy at low levels (McNamara & Nulsen 2012). Radiative AGN feedback, on the other hand, has been mostly associated with luminous AGN (i.e. Quasars, $L_{\mathrm{X}} \gtrsim 10^{45}$ erg s^{-1}) at intermediate to high redshifts ($z \gtrsim 0.5$), where galaxy-wide AGN-driven winds (with

★ E-mail: daniel.ruschel@ufsc.br

© 2021 The Author(s)
Published by Oxford University Press on behalf of Royal Astronomical Society

Downloaded from https://academic.oup.com/mnras/article/507/1/74/6324028 by Universidade Federal do Rio Grande do Sul user on 15 October 2021

typical extensions of 1–10 kpc) have been observed both in warm ionized and cold molecular gas (Cicone et al. 2014; Harrison 2014; Leung, Riechers & Pavesi 2017; Vayner et al. 2017; Herrera-Camus et al. 2019; Davies et al. 2020). These winds can sweep away or heat up large amounts of gas, shutting off star formation in the host galaxy Dall'Agnol de Oliveira et al. (2021).

A number of studies focusing on the star formation properties of Quasars, however, paint a different picture: Quasars are found to have similar star formation rates to main-sequence galaxies at the same redshift (Harrison et al. 2012; Stanley et al. 2015; Ramasawmy et al. 2019; Schulze et al. 2019), implying no evidence of enhancement or suppression of star formation. These apparently conflicting results can be reconciled if the time-scale for suppression of star formation is longer than the time-scale of AGN activity (Hickox et al. 2014; Harrison 2017; Rodighiero et al. 2019). In this case, theoretical predictions will need to be combined with observations to identify the effects of AGN feedback (see Scholtz et al. 2018 for a discussion). Thus, it is critical to constrain how the energy radiated by the AGN couples to the host interstellar medium and determine the efficiency of this coupling, so that AGN feedback is properly implemented in numerical simulations and semi-analytical models.

While the most energetic AGN-driven winds are observed in distant Quasars, they are not the most adequate targets to quantify the impact of AGN radiative feedback on the evolution of the general galaxy population. This is because Quasars are not representative of the bulk of the AGN population, which is comprised mainly of moderate luminosity AGNs ($L_X \approx 10^{42}$–10^{44} erg s^{-1}, i.e. Seyfert galaxies), as evidenced by high-redshift X-Ray surveys (Brandt & Alexander 2015). Ideally one should study AGNs with redshifts in the range $z \sim 1$–3, as this is the epoch where both the star formation rate density and black hole accretion density peak. However, this is not feasible, as in moderate luminosity AGNs winds typically do not extend beyond the inner 1 kpc, so they would be unresolved with current observational facilities. It is thus necessary to find local Universe analogues that still serve as subjects for the study of feedback mechanisms.

In order to be able to resolve the inner kpc of moderately active galaxies, our group AGNIFS (AGN Integral Field Spectroscopy) has observed over the years several AGN hosts using Gemini IFS in the optical (e.g. Fathi et al. 2006; Storchi-Bergmann et al. 2007; Barbosa et al. 2009; Schnorr-Müller et al. 2014b; Lena et al. 2015; Schnorr-Müller et al. 2016, 2017a, b; Brum et al. 2017; Freitas et al. 2018; Humire et al. 2018; Slater et al. 2019; Muñoz-Vergara et al. 2019; Soto-Pinto et al. 2019) and in the near-IR (Storchi-Bergmann et al. 2009, 2010; Riffel et al. 2017, 2018; Schönell et al. 2019). While we have so far focused on individual galaxies, in this paper we present data for 30 objects observed in the optical using the Gemini Multi-Object Spectrograph Integral Field Unit (GMOS-IFU). For these we homogeneously derive maps of the gas emission-line fluxes, flux ratios and kinematic properties. Our main goal is to probe the gas excitation and kinematics within the inner kiloparsec of the host galaxies at spatial resolution down to tens to hundreds of parsecs in order to resolve the relevant processes of feeding and feedback of the AGN at the nucleus. In this first paper, we also report the values we have obtained for the galaxy photometric major axis, kinematic major axes of the gas and stellar kinematics, as well as mass-outflow rates and powers obtained from the measurements of emission-line profile widths at 80 per cent intensity (W_{80}) when such values exceed 600 km s^{-1}. We also compare our results with those of previous studies relating these quantities to the AGN luminosity (e.g. Fiore et al. 2017).

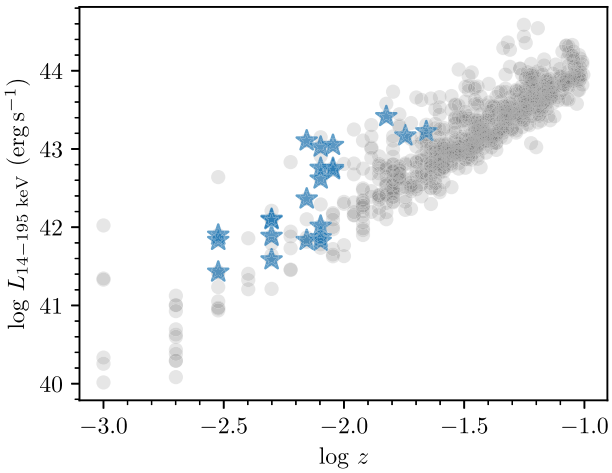

Figure 1. The location of the 22 galaxies of our sample which are listed in the *Swift*/BAT 105 month sample are shown as blue stars in this luminosity versus redshift plane. Grey circles are *Swift*/BAT sources and blue stars are the 22 targets that overlap that sample in this paper.

This paper is structured as follows: in Section 2 we discuss the sample, Section 3 deals with the observations and data reduction procedures, emission-line analysis and fitting is discussed in Section 4, general results are shown in Section 5, outflow estimates and comparison to AGN properties are shown in Section 6 and finally we present our conclusions in Section 7.

2 THE SAMPLE

The sample comprises 30 AGNs, primarily in late-type galaxies, observed with the Gemini instruments GMOS-IFUs (North and South), between 2010 and 2017, and limited to a redshift of $z \leq 0.01$, except for three sources (Mrk 1058, Mrk 6, and Mrk 79) that are at $z \approx 0.02$. Out of the 30 galaxies in the sample, 22 have a counterpart in the 105 month *Swift*/BAT (hereafter SB105) catalogue (Oh et al. 2018). A target in our sample is considered to have a counterpart in SB105 if it lies within 15 arcmin of an X-Ray source. Incidentally, all the 22 counterparts in SB105 are classified as AGNs. The remaining eight galaxies without a bright X-ray counterpart are either LINERS or Seyfert 2's (Sy2). Fig. 1 shows the location of our sample galaxies (blue stars) in the redshift–luminosity plane, along with other sources from the SB105 catalogue (grey circles). The 19 shared targets below $z = 0.01$ in our sample correspond to nearly a third of all Seyfert and LINER galaxies detected by *Swift*/BAT in that volume.

With the advent of recent surveys on black hole masses ($M_\bullet$) we can assess how well are we sampling the population of SMBHs in terms of their masses. In Fig. 2, we compare the $M_\bullet$ distribution of our sample and the complete sample from van den Bosch (2016). We can see that, in comparison to that sample, our targets are lacking in the high-mass end.

Basic properties of the galaxies studied in this paper are listed in Table 1. The nuclear activity type is based on Véron-Cetty & Véron (2010), and our re-evaluation is based on the nuclear spectra, where S1, S2, L1, and L2 represent Seyfert 1, Seyfert 2, Liner 1, and Liner 2, respectively. Most of the distances were taken from Tully et al. (2013), which is a compilation of measurements based on six different redshift-independent methods. When more than one method was available, the average was adopted. No redshift-independent distance method could be found for the galaxies MCG -05-23-015

Downloaded from https://academic.oup.com/mnras/article/507/1/74/6324028 by Universidade Federal do Rio Grande do Sul user on 15 October 2021

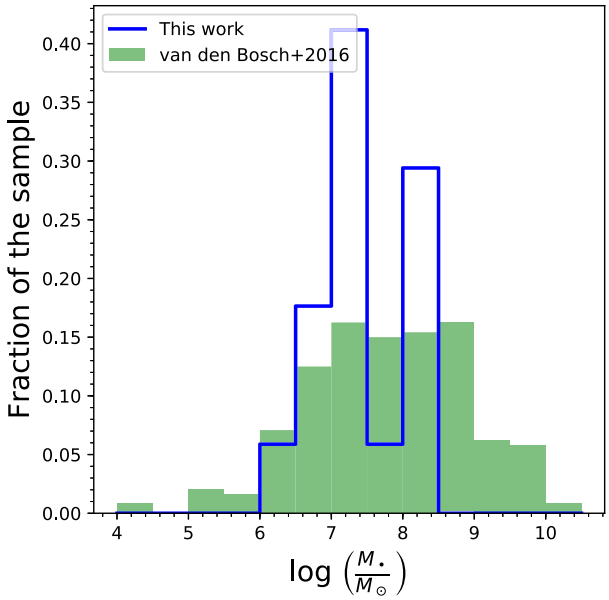

Figure 2. Histogram of the black hole masses of our sample galaxies compared to that compiled by van den Bosch (2016). Our sample shows a narrower distribution – covering masses in the range 10^6–$10^{8.5}$ $M_\odot$ and missing the high-mass end of the distribution ($10^{8.5}$–10^{10} $M_\odot$).

Table 1. Sample properties: activity type, morphology, distance, and projected scale.

Galaxy	Act.	Morph.	Distance Mpc	Scale (pc arcsec^{-1})
Mrk 348	S2	SA(s)0/a:	21.5	104
NGC 1068	S2	(R)SA(rs)b	12.6	61
Mrk 1058∗	S2	S?	72.8	346
Mrk 607	S2	Sa	37.7	181
NGC 1365	S1	SB(s)b	18.1	87
NGC 1358∗	S2	SAB0/a(r)	56.0	267
NGC 1386∗	S2	SB0^+(s)	15.9	77
NGC 1566	S1	SAB(s)bc	6.6	32
NGC 1667∗	S2	SAB(r)c	42.8	205
NGC 2110	S2	SAB0^-	36.9	177
Mrk 6	S1	SAB0^+:	95.0	449
Mrk 79	S1	SBb	90.5	428
NGC 2787∗	L2	SB0^+(r)	7.4	36
MCG -05-23-016	S1	S0?	41.3	198
NGC 3081	S2	(R)SAB0/a(r)	32.5	156
NGC 3227	S1	SAB(s)a pec	20.6	99
NGC 3516	S1	(R)SB0^0?(s)	38.9	187
NGC 3783	S1	(R')SB(r)ab	38.5	185
NGC 3786	S2	SAB(rs)a pec	47.0	225
NGC 3982∗	S2	SAB(r)b?	21.6	104
NGC 4180	S2	Sab?	37.5	180
NGC 4450∗	L1	SA(s)ab	15.3	74
NGC 4501∗	S2	SA(rs)b	19.7	95
NGC 4593	S1	(R)SB(rs)b	25.6	123
MCG -06-30-015	S1	S?	37.4	180
NGC 5728	S2	SAB(r)a?	26.4	127
NGC 5899	S2	SAB(rs)c	45.3	217
NGC 6300	S2	SB(rs)b	14.0	68
NGC 6814	S1	SAB(rs)bc	22.8	110
NGC 7213	S1	SA(s)a?	22.0	106

Note. '∗' indicates galaxies with an X-Ray counterpart in *Swift*/BAT 105 month catalogue (Oh et al. 2018).

and MCG -06-30-16; for these we based our distance calculation on the redshift with respect to the cosmic microwave background.

Projected scales were evaluated from the distances assuming the cosmological parameters from Hinshaw et al. (2012) ($H_0 = 69.32$ km s^{-1} Mpc^{-1}, $\Omega_\Lambda = 0.7135$, and $\Omega_m = 1 - \Omega_\Lambda$) and a flat ΛCDM model. They range from 32 pc arcsec^{-1} for NGC 1566 up to 449 pc arcsec^{-1} for Mrk 1058. Regarding the environment, only two of the galaxies in our sample are known to be interacting with another galaxy: NGC 3227 (Mundell et al. 2004) and NGC 3786 (Noordermeer et al. 2005). Additionally, the galaxy NGC 2110 shows a prominent dust lane, which may be an indication of a recent merger (Drake et al. 2003).

Finally, we point out that many galaxies in this sample have been individually presented in previous papers of the AGNIFS group, as pointed out in the Introduction. The main difference between those studies and the present paper is that here we performed a homogeneous analysis of the whole sample, with a uniform methodology. Our aim is to use as few target specific assumptions as possible, in order to form an internally consistent picture across this sample of galaxies.

3 OBSERVATIONS AND DATA REDUCTION

3.1 Observations

The data used in this study come from many observing runs, although with similar set-ups, obtained with the GMOS-IFUs (Allington-Smith et al. 2002) both at the northern and southern Gemini telescopes. These IFUs consist of up to 1500 lenslets that feed the light, via fibre optic cables, to the diffraction grating. Each lenslet, which is hexagonal in shape, has a projected diameter in the plane of the sky of 0.″18.

GMOS has two modes of IFS observation: a 'single slit' mode which provides a field of view (hereafter FoV) of 3.5 × 5 arcsec, and spectral coverage of ∼2000 Å, and a 'two slit' mode which trades roughly half the spectral coverage for a doubled FoV. The slits mentioned here are not actual slits, but rather the result of arranging the fibres in a straight line. In the single slit mode each exposure produces 500 on-source spectra, and 250 sky spectra. The latter are used to remove atmospheric emission from the science spectra. These numbers are doubled in the two slit mode.

The gratings used in these observations, namely B600 and R400, have a resolving power of $R \sim 1800$, which translates to a velocity resolution of ∼50 km s^{-1}. [O III] and H β lines are available only for the 13 galaxies of the sample observed in single slit mode, covering the wavelength range ≈ 4800–7000 Å, and identified in Table 2 with the symbol † adjacent to its name while the remaining targets were observed in two-slit mode and have spectra in the range ≈ 5600–7000 Å. Angular resolutions vary between 0.″6 and 1.″0, depending on the seeing.

Fig. 3 shows examples of the IFU's FoV superimposed on the *r*-band acquisition images. The bottom panel displays the nuclear spectrum of each galaxy, summed over a circular aperture with a 1 arcsec radius. The acquisition images with the superimposed IFU FoVs of all other galaxies in the sample are shown in Fig. B1 of Appendix B (Supporting Information).

3.2 Data reduction

Data reduction was based on the package provided by the Gemini observatory for IRAF. Additionally, we have developed a publicly

Downloaded from https://academic.oup.com/mnras/article/507/1/74/6324028 by Universidade Federal do Rio Grande do Sul user on 15 October 2021

Table 2. Observation log – Columns are: (1) galaxy name; (2) Gemini program ID; (3) on-source exposure time in seconds; (4) field of view in arcsec.

Galaxy	Program ID	Exp. time	FoV
Mrk 348†	GN-2014B-Q-87	4860	1.7 × 2.5
NGC 1068†	GS-2010B-Q-81	2491	3.3 × 4.9
Mrk 1058†	GN-2014B-Q-87	4860	1.7 × 2.5
Mrk 607†	GN-2014B-Q-87	4860	1.7 × 2.5
NGC 1365†	GS-2014B-Q-30	1890	3.3 × 5.3
NGC 1358	GS-2010B-Q-19	4206	7.4 × 9.5
NGC 1386	GS-2011B-Q-23	4506	7.4 × 9.5
NGC 1566	GS-2011B-Q-23	4506	7.4 × 9.5
NGC 1667	GS-2010B-Q-19	4206	7.4 × 9.5
NGC 2110	GS-2010B-Q-19	4206	7.4 × 9.6
Mrk 6†	GN-2014B-Q-87	5670	3.4 × 5.1
Mrk 79†	GN-2014B-Q-87	4860	1.7 × 2.5
NGC 2787	GN-2011A-Q-85	4920	7.1 × 9.2
MCG -05-23-016†	GS-2014A-Q-78	2400	6.3 × 5.5
NGC 3081	GN-2011A-Q-85	4920	7.1 × 9.2
NGC 3227†	GN-2013A-Q-61	2400	6.3 × 4.9
NGC 3516†	GN-2013A-Q-61	7201	9.3 × 4.9
NGC 3783†	GS-2014A-Q-78	4802	6.3 × 5.8
NGC 3786†	GN-2013A-Q-61	4800	6.3 × 4.9
NGC 3982	GN-2006B-Q-94	4680	7.4 × 15.5
NGC 4180	GN-2014A-Q-90	4800	6.3 × 5.8
NGC 4450	GN-2006B-Q-94	4682	21.4 × 5.5
NGC 4501	GN-2008A-Q-8	6000	7.4 × 15.5
NGC 4593†	GN-2013A-Q-61	4800	6.3 × 4.9
MCG -06-30-015†	GS-2014A-Q-78	4802	6.3 × 5.8
NGC 5728†	GS-2013A-Q-56	4802	6.3 × 4.9
NGC 5899†	GN-2013A-Q-61	6818	6.7 × 5.0
NGC 6300†	GS-2014A-Q-78	8823	6.8 × 5.8
NGC 6814†	GS-2014A-Q-78	2400	6.3 × 5.6
NGC 7213	GS-2011B-Q-23	4506	7.4 × 9.5

Note. '†' indicates galaxies observed in single slit mode.

available automated pipeline named GIREDS[1] to process the raw data through the many tasks of the Gemini package, and also perform quality control checks along the reduction. The reduction follows standard procedures of bias subtraction, flat-fielding and wavelength calibration based on arc lamp spectra. Spectra from each fibre were extracted using apertures identified in the flat-field images, which were taken within 2 h from the science images. Relative flux calibration was achieved using spectrophotometric stars observed in the same semester of the science observations, and the same instrumental set-up

In order to facilitate posterior analyses of the data cubes, GMOS' original IFU matrix, which is composed of hexagonal lenslets with a diameter of 0.″18, was interpolated into an image with square spaxels, each having a side of 0.″1. This process causes a minor oversampling of the data but allows the direct application of standard image analysis tools over the data cube. The task GFCUBE was used in resampling the data cube, which includes a correction for differential atmospheric refraction for each wavelength plane.

Gemini's world coordinate system (WCS) uncertainty and repeatability are comparable to the IFU FoV (∼5 arcsec), thus one cannot rely on the WCS data for combining data cubes with spatial dithering. Since these observations were not performed using adaptive optics, the spatial resolution element is seeing limited to a full width at half-maximum (FWHM) of 0.″6 at best. Therefore, registering of different exposures of the same galaxy based on the peak of continuum emission would most probably degrade the spatial resolution. The best results were achieved by combining data cubes from different observations based on instrumental offset coordinates.

[1]https://github.com/danielrd6/gireds

3.3 Flux calibration

The majority of the data cubes in our sample do not have an associated observation of a standard spectro-photometric star. We therefore resorted to a method of absolute flux calibration based on the acquisition images. The method consists in matching stars of known magnitude, taken from an astrometric catalogue, to point sources that appear within the FoV of the acquisition camera.

Acquisition images were first reduced using the Gemini IRAF package for GMOS image reduction. Using the Astrometry.net software (Lang et al. 2010), we have re-generated the astrometric calibration of each acquisition image, in order to ensure that we are matching the correct sources to the correct stars in the catalogue. Aperture photometry was performed using the PHOTUTILS package (Bradley et al. 2018), with stellar sources being identified by a Python implementation of the DAOFIND algorithm (Stetson 1987). Stellar magnitudes and positions were taken from the USNO-B catalogue (Monet et al. 2003), which has typical *R*-band magnitude uncertainties of 0.25 mag. In principle, performing flux calibration with the acquisition images should account for all low-frequency atmospheric effects, since the acquisition is taken within 2 h or less of all the science exposures.

Zero-point magnitudes for the acquisition images were evaluated as the median of equation (1) for all the *i* stellar sources identified in the acquisition image. Sources with FWHM which differed by more than 20 per cent of the median FWHM were rejected. An iterative sigma-clipping algorithm was also used to reject outliers above the 3σ level:

$$\mu_i = 2.512 \log I_i + m_i, \quad (1)$$

where μ_i is the magnitude zero-point, I_i is the background-subtracted instrumental flux from the aperture photometry, and m_i is the magnitude in the USNO-B catalogue. Since all acquisition images were taken with the filters G0326 and G0303 (for Gemini's South and North respectively), we chose to use the relatively similar *R*-band magnitudes of USNO-B. The flux ratio between the Johnson *R* band and GMOS' filters is reasonably stable for a wide variety of stellar spectra, which we tested with the MILES library (Falcón-Barroso et al. 2011), with a standard deviation of 12 and 5 per cent for G0303 and G0326, respectively.

Once we have the estimate for the conversion of instrumental units to *R*-band magnitudes, we proceeded to perform a spectrophotometric analysis of the data cube. A nuclear spectrum was extracted from the IFS data, using a circular aperture with 1 arcsec of radius, centred on the peak continuum emission. The equivalent *R*-band magnitude of this spectrum was estimated by multiplying the spectrum by the filter transmission curve and integrating over wavelength. Comparing the latter to the magnitude obtained within an identical aperture in the acquisition image yielded a conversion factor from the relative flux to the absolute flux.

4 EMISSION-LINE FITTING

The emission-line measurements are based on the fit of a combination of Gauss–Hermite polynomials (van der Marel & Franx 1993; Riffel 2010) up to the fourth order with a number of constraints among related spectral lines. Gauss–Hermite polynomials have the

Downloaded from https://academic.oup.com/mnras/article/507/1/74/6324028 by Universidade Federal do Rio Grande do Sul user on 15 October 2021

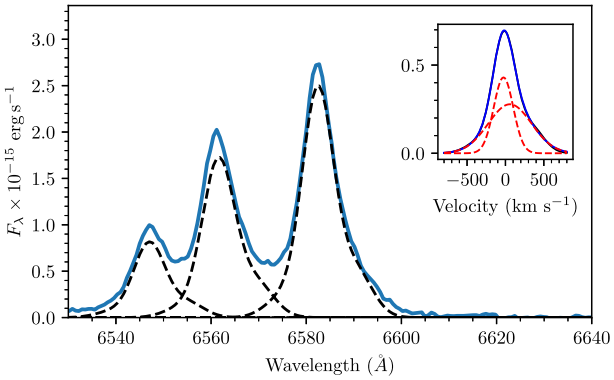

Figure 4. Emission-line modelling example (nuclear region of NGC 2110) showing only the narrow component of H α and the [N II] lines. In this example $h_3 = 0.06$ and $h_4 = 0.09$, indicating the presence of a red wing in the profile. This line profile can also be represented by a two-Gaussian fit, which is shown in the inset plot.

advantage of reduced dimensionality in comparison to multicomponent Gaussian fits. However, the function itself is not physically motivated, and therefore the quantitative interpretation of the results is comparatively more complex. In addition to the amplitude, mean and standard deviation parameters of a single-Gaussian curve, we fitted the coefficients h_3 and h_4 for the third and fourth-order elements, respectively. The effect of the h_3 coefficient is to produce an asymmetric profile, with positive values having a blue wing, and negative values having a red wing. The h_4 profile, on the other hand, produces a symmetric effect of broadening the base of the profile for positive value, or the top for negative values. An example of such a fit and its interpretation in light of a double-Gaussian profile is shown in Fig. 4.

Profile fitting of emission lines was done by an in-house developed algorithm. This code is part of a PYTHON based package of spectral analysis routines, named IFSCUBE (Ruschel-Dutra & Dall'Agnol de Oliveira 2020), which is publicly available on the internet. IFSCUBE allows the fitting of Gaussian or Gauss–Hermite profiles, with or without constraints or bounds. The fitting algorithm includes integrated support for pixel-by-pixel uncertainties, weights and flags, subtraction of stellar population spectra, pseudo-continuum fitting, signal-to-noise ratio evaluation, and equivalent width measurements. Model fitting relies on SCIPY'S (Virtanen et al. 2020) routines for nonlinear numerical minimization. IFSCUBE also supports user interaction via a human-readable configuration file, allowing even those that are unfamiliar with the Python language to use it. The stellar population contribution was fit to the spectrum with spectral synthesis code pPXF (Cappellari & Emsellem 2004; Cappellari 2017) and the MILES simple stellar population models (Vazdekis et al. 2010). For the few galaxies in which the signal-to-noise ratio in the stellar continuum was not high enough to reliably constrain the stellar population, the continuum was represented by a smooth polynomial function.

In Type 1 AGNs the broad component of the hydrogen lines was fitted by a combination of three Gaussian curves, in tandem with two Gaussian curves for each of the narrow lines. The central wavelength, relative flux, and width of each of the three Gaussian components were fit only once, using the summed spectrum of all the spaxels within 1 arcsec from the continuum centre. Since the broad H lines originate in the same unresolved source, we can apply the same model for all the spectra with the broad-line contribution, with only a scaling factor for the flux. Having constrained the broad components in this way, the narrow components were fitted again over the whole data cube.

Fig. 4 shows an example of the emission-line modelling for the nuclear spectrum of NGC 2110. In this example each individual component is shown as a dashed black line and the observed spectrum, minus the stellar population, as a solid blue line. The broad H α component was omitted here to emphasize the profiles of the narrow lines. A representation of the Gauss–Hermite polynomial fit in terms of a two-component Gaussian model is shown in the inset at the upper right of Fig. 4.

Assuming the narrow-line region to be in ionization equilibrium, and to be well represented by the case B recombination scenario (Osterbrock & Ferland 2006), we imposed the corresponding constraint on the flux ratio of the [N II] lines F[N II] λ6548/F[N II] λ6583 = 1/3. Kinematic parameters for the [N II] and [S II] lines are kept the same, namely the velocities corresponding to the line centres and the velocity dispersion with respect to the rest frame, as well as the h_3 and h_4 parameters. These last two parameters were also limited to values between −0.2 and +0.2. When the blue portion of the spectrum was available, the following constraints were also used: fixed kinematics and between [O III] lines and between H α and H β, and also a fixed ratio of $f_{5007}/f_{4959} = 3$ for the [O III] lines. The flux ratio between the [S II] lines at $\lambda\lambda$6716, 6731 Å was constrained within the lower and upper electron density limits: $0.41 < f_{6716}/f_{6731} < 1.45$.

4.1 Velocity dispersion via W_{80}

Traditional quantities to represent the velocity dispersion of a quasi-Gaussian profile, such as the Gaussian σ or the FWHM, fail to capture the complex kinematic picture that is commonly encountered in AGN, in particular at high velocity dispersion. Therefore we employed the W_{80} index (Zakamska & Greene 2014), which is the width, in velocity scale, that encompasses 80 per cent of the flux of a given emission line. This index has the advantage of being independent from the assumed line profile, since it is measured directly on the observed profile. Assumptions about the line profile are only important when measuring the W_{80} index of a blended line, as neighbouring lines have to be subtracted prior to the integration.

The W_{80} evaluation begins with the subtraction of the continuum – the fitted stellar population templates or a local continuum in the cases we could not fit the stellar population – and also of neighbouring emission lines, when applicable. Then a cumulative integral is calculated and normalized, so that the W_{80} will be the difference between the velocity at 90 per cent and 10 per cent of the total flux. The integration limits for the cumulative integral are set at $\pm 5\sigma$ from the line centre, which was evaluated during the profile fitting process. For a Gaussian profile W_{80} is about 10 per cent larger than the FWHM, or $W_{80} = 2.56 \times \sigma$. Normal rotation velocities and velocity dispersions for a galactic potential of even the most massive galaxies limits the W_{80} to 600 km s^{-1}. Emission lines with $W_{80} >$ 600 km s^{-1} are therefore a signature of gas in unbound orbits, most probably (and assumed to be the case here) outflowing (e.g. Harrison 2014; Sun, Greene & Zakamska 2017)

Some emission-line profiles, most notably the Hydrogen lines of the Balmer series, are affected by the underlying stellar absorption, which influences both the flux and the centre of the ionized gas features. This has been taken care of with the fit and subtraction of the stellar population contribution, except for the Markarian galaxies for which the stellar continuum is too weak and this fit and subtraction was not possible. For these galaxies, with no stellar population

Downloaded from https://academic.oup.com/mnras/article/507/1/74/6324028 by Universidade Federal do Rio Grande do Sul user on 15 October 2021

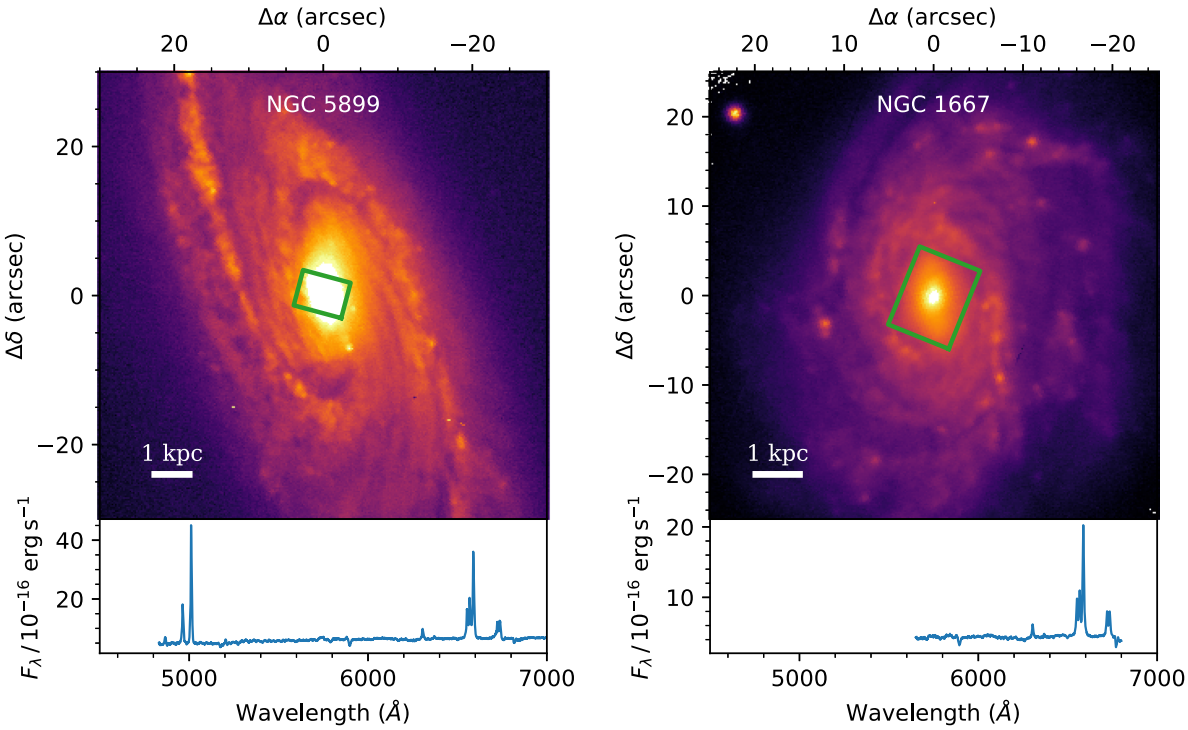

Figure 3. Upper panels: acquisition images of NGC 5899 and NGC 1667, where the rectangle shows the GMOS-IFU FoV and the white bar shows the scale at the distance of the galaxy. Lower panels: the summed spectrum of the central 1 arcsec radius in arbitrary flux units and wavelengths in Å.

subtraction, we impose a lower limit on the equivalent width of Hα emission of W_λ(Hα) > 6 Å when estimating the Hα luminosities. The reason is that this value corresponds to approximately twice the maximum absorption W_λ(Hα) of any simple stellar population (e.g. Bruzual & Charlot 2003), thus corresponding to a possible maximum error of about 30 per cent in the emission-line flux.

5 RESULTS

Results in the form of maps obtained from the emission-line fits, as well as of some derived properties, are shown in Fig. 5, Figs C1–C30 of Appendix C (Supporting Information) and in Table 3. Fig. 5 is an example, showing the galaxy Mrk 348, with a spectral coverage of ≈4800–7000 Å; however, almost half of our sample is limited to the range ≈5600–7000 Å. The former allows the mapping of the [O III] and Hβ emission-line properties besides those of Hα + [N II] and [S II] of the latter.

The maps in the above figures show: the flux distribution of a selected ionized gas emission line ([N II] and [O III] when available); the radial velocity of the ionized gas, given by the central wavelength of the emission-line fit; the W_{80} map; the equivalent width of the narrow component of Hα; the flux ratios between [N II] ([O III] when available) and Hα (Hβ when available); and the electron density of the ionized gas. The latter is based on the flux ratio between the [S II] λλ6716, 6731 Å lines (see Section 6.4). All figures were rotated so that North is up and East is to the left. In order to remove high-frequency noise from the images, we have convolved them with a 2D Gaussian kernel, with $\sigma = 0.2$ arcsec, corresponding to approximately the size of the lenslet in the IFU array, and two spaxels of the data cube. The cross in the centre of the images marks the peak of stellar continuum emission, which we adopted as corresponding to the galaxy nucleus. In order to better visualize the flux distributions of the emission lines, we have defined the 'strong emission region' (SER) as that enclosed by an isophote with a flux level 1/10th of the peak flux; shown in the in the flux maps (upper left panel of the figures) as the dashed light green contour. Only continuously connected emitting regions with origin at the galactic nucleus are considered, thus excluding ionized gas clouds that are not directly connected to the nucleus.

We have also included in the figures a dashed red line showing the orientation of the photometric major axis (hereafter PMA) determined over a 2MASS *K*-band image except for the galaxies NGC 1068, NGC 1566, NGC 4593 which were individually evaluated based on DSS images, and NGC 5728 which follows Erwin (2004). The orientation of the PMA is also listed in Table 3.

The magenta dashed line in the figures shows the approximate direction of elongation of the area dominated by outflows when present, as visually inferred from the gas kinematic and flux distribution maps (these latter showing the orientation of the ionization axis). The adopted outflow PA is listed in the eighth column of Table 4. In some cases for which there is no clear indication of outflow along the ionization axis, but there is enhancement in W_{80} perpendicular to the ionization axis, we have adopted this PA as corresponding to the outflow. We have also included in the W_{80} maps a dashed circle showing the distance at which we have calculated the mass-outflow rates and powers, which are also listed in the second and fourth columns of Table 4.

Table 3 also includes the kinematic major axis derived from the [N II] and [O III] velocity fields, which is represented by the blue continuous line in Fig. 5. Position angles for the kinematic axes were inferred based on the assumption of a symmetric velocity field, and using the FIT_KINEMATIC_PA code (Krajnovic et al. 2006). Although not as justifiable as in the [N II] case, assuming a symmetric [O III] velocity field is still informative for our purposes, if only in

Downloaded from https://academic.oup.com/mnras/article/507/1/74/6324028 by Universidade Federal do Rio Grande do Sul user on 15 October 2021

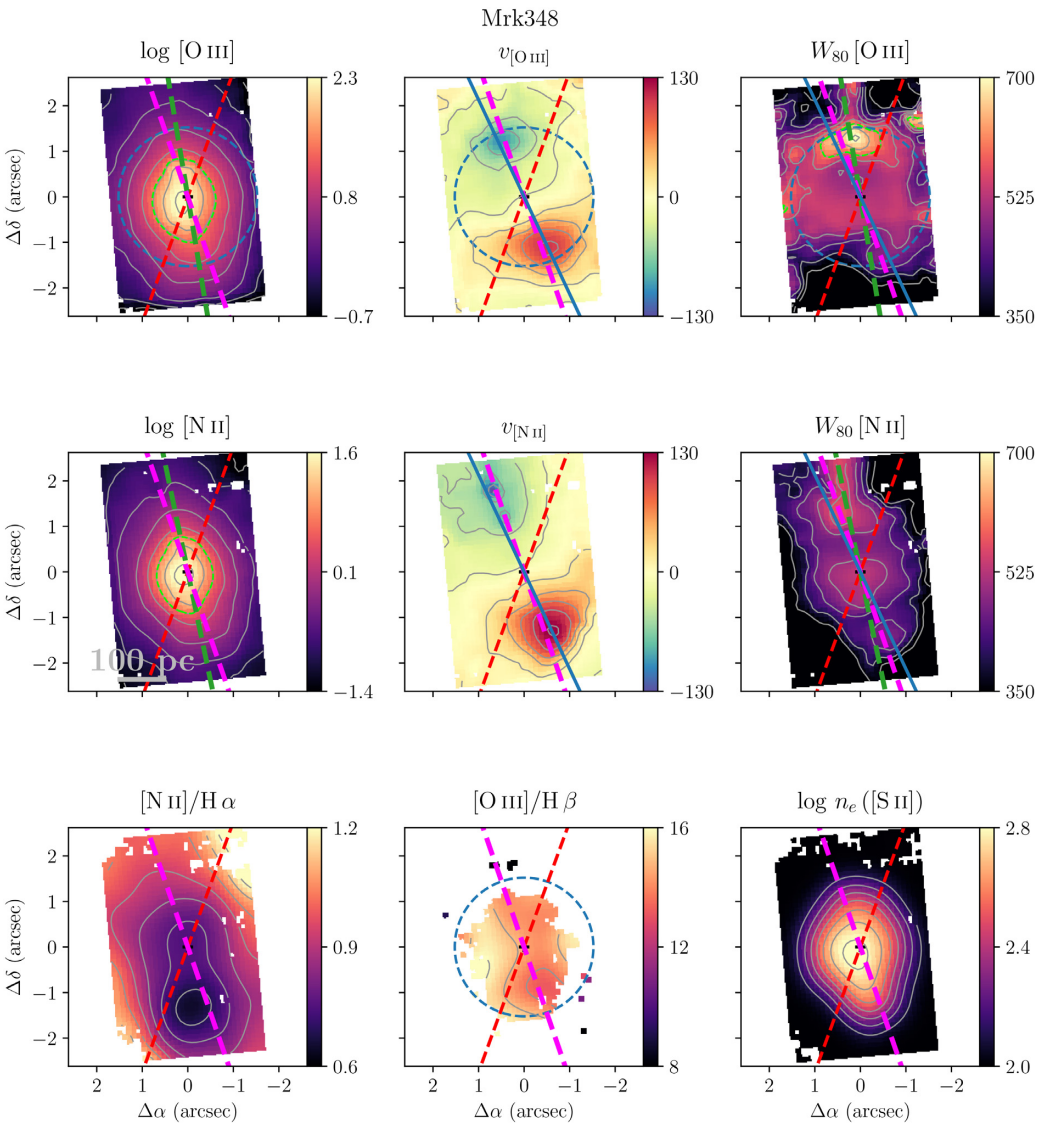

Figure 5. Summary of results for Mrk 348. The bar in the lower left of the [N II] flux panels represents the projected scale. The colour coding is in units of $\log_{10}(F \times 10^{-15}$ erg s^{-1} cm^{-2}) for the line fluxes, km s^{-1} for the velocities and W_{80}, Å for the equivalent width and $\log_{10}(n_e \times$ cm^3). The systemic velocity of the galaxy, inferred from the ionized gas velocity field, has been subtracted from the radial velocity of the emission lines. Markings in the maps are as follows: red dashed line: orientation of the photometric major axis; blue dashed line: orientation of kinematic major axis; green contours: in the [N II] and [O III] flux panels enclose the region with 10 per cent of the total flux and in the W_{80} map the region with values higher than 600 km s^{-1}; blue dashed circle: the distance used to estimate the mass-outflow rate and kinetic power; green dashed line: ionization axis; magenta dashed line: direction of elongation of the outflow dominated area. This figure is also displayed in Appendix C (Supporting Information).

a comparative sense. Furthermore, a symmetric velocity field does not necessarily imply rotation, since it could also be the result of a biconical outflow. Fits of the [N II] velocity field were used to derive the gas systemic velocities of each galaxy, which were subtracted from the velocity maps and are listed in the second column of Table 3. These same velocity field fits also give the kinematic major axis for each emission line (third and sixth columns).

We now discuss the global properties of the sample.

5.1 Flux maps and excitation

Inspection of the flux maps in Fig. 5 and Figs C1–C30 of Appendix C (Supporting Information) reveals extended emission over most of the FoV and some degree of collimation along a direction that we identify as the ionization axis. The orientation of the ionization axis varies; for the following 10 galaxies this orientation is similar to the PMA: Mrk 607, NGC 1365, NGC 1566, NGC 1667, NGC 2110, MCG-05-23-016, NGC 3516, NGC 3786, NGC 4593, and MCG-06-30-015. Collimated gas emission along a direction distinct from that of the PMA is observed in 15 galaxies: Mrk 348, Mrk 1058, NGC 1068, NGC 1358, NGC 1386, Mrk 6, Mrk 79, NGC 2787, NGC 3081, NGC 3227, NGC 4501, NGC 5728, NGC 5899, NGC 6300, and NGC 6814. In the case of the following 5 galaxies: NGC 3783, NGC 3982, NGC 4180, NGC 4450, and NGC 7213, the orientation of the ionization axis is not clear.

The line ratios [O III]/H β and [N II]/H α are all consistent with AGN excitation over most of the FoVs. Only occasionally their values indicate that ionization from young stars becomes dominant in the vicinity of the AGN (i.e. in the galaxies NGC 1566 and NGC 2110).

Downloaded from https://academic.oup.com/mnras/article/507/1/74/6324028 by Universidade Federal do Rio Grande do Sul user on 15 October 2021

Table 3. Velocities, kinematic and photometric major axis – Columns are: (1) name of the galaxy; (2) systemic velocity of the [N II] velocity field; (3) kinematic major axis of the [N II] velocity field; (4) [N II] ionization axis; (5) systemic velocity of the [O III] velocity field; (6) kinematic major axis of the [O III] velocity field; (7) [O III] ionization axis; (8) Photometric major axis.

Galaxy	[N II] v_{sys} (km s^{-1})	KMA [N II] (°)	[N II] IA	[O III] v_{sys} (km s^{-1})	KMA [O III] (°)	[O III] IA	PMA (°)
Mrk 348	4531	25	12	4529	25	9	160
NGC 1068	1009	23	9	984	28	18	82†
Mrk 1058	5102	127	27	5089	167	18	115
Mrk 607	2777	133	139	2750	131	140	140
NGC 1365	1617	60	153	–	–	–	49
NGC 1358	4083	84	124	–	–	–	15
NGC 1386	822	22	7	–	–	–	25
NGC 1566	1469	33	30	–	–	–	40†
NGC 1667	4641	138	159	–	–	–	165
NGC 2110	2344	172	167	–	–	–	165
Mrk 6	5526	166	8	5628	171	36	130
Mrk 79	6625	147	8	6618	31	5	65
NGC 2787	672	68	75	–	–	–	110
MCG -05-23-016	2537	66	66	2549	72	157	50
NGC 3081	2412	75	143	–	–	–	70
NGC 3227	1122	0	171	1041	14	175	153
NGC 3516	2608	36	10	2621	24	13	27
NGC 3783	2969	75	15	–	–	–	100
NGC 3786	2682	74	82	2685	75	90	70
NGC 3982	1107	25	34	–	–	–	15
NGC 4180	2042	177	52	–	–	–	20
NGC 4450	1920	36	84	–	–	–	0
NGC 4501	2238	124	160	–	–	–	140
NGC 4593	2485	95	115	2489	83	125	120†
MCG -06-30-015	2325	117	112	2323	111	109	115
NGC 5728	2772	173	143	2812	172	148	2†
NGC 5899	2671	49	177	2672	9	176	20
NGC 6300	1111	161	58	1089	24	61	118
NGC 6814	1637	170	135	1667	144	148	65
NGC 7213	1859	128	159	–	–	–	70

Note. Photometric major axis for most galaxies is taken from the 2MASS Extended Source Catalog (XSC), with the exception of those marked with †. For NGC 5729 the PA was taken from Erwin (2004), and for the remaining three the PA was visually estimated from the DSS images.

5.2 Velocity fields and W_{80} maps

Most velocity fields are dominated by a rotation component, consistent with the 'S' (spiral) morphology type of the galaxies as listed in the first column of Table 1. This rotation pattern can be seen in the individual velocity maps in Appendix C (Supporting Information), and its orientation was determined based on the assumption of a symmetric velocity field (see Section 5). But in most cases the rotation pattern is disturbed due to the presence of non-circular motions, as described below. The nature of this non-circular component has been investigated in previous studies by our group for a number of individual cases, as discussed in Appendix A (Supporting Information), being associated with inflows along nuclear spirals and/or to outflows. In this section we point out signatures of outflows in the gas velocity fields and W_{80} maps, using W_{80} as an indicator of the mechanical feedback of the outflows in the host galaxy. A further analysis of the gas kinematics is deferred to a forthcoming paper where we will present modelling of the gas velocity fields and their comparison with the stellar velocity field.

Inspection of the velocity fields and W_{80} maps show that in five cases – Mrk 348, NGC 1068, NGC 3227, NGC 3516, and NGC 5728 – increased W_{80} values – reaching $W_{80} \geq 600$ km s^{-1} surround regions of blue and redshifts to both side of the nucleus where steep velocity gradients are observed along the ionization axis and can be interpreted as due to outflows. We interpret the increase in W_{80} as compression of the surrounding gas by the passing outflow. There are some cases in which an increase in W_{80} is also observed in association to blue and redshifts along the ionization axis but which do not produce $W_{80} \geq 600$ km s^{-1}: Mrk 1058, NGC 4501, and NGC 6814.

Increase in the values of W_{80}, reaching $W_{80} \geq 600$ km s^{-1}, not along but approximately perpendicularly to the ionization axis have been found in another five cases: NGC 1386, NGC 2110, Mrk 6, Mrk 79, and NGC 5899. Our interpretation in these cases is a lateral expansion of the surrounding gas by an outflow or radio jet. The cases in which the increase of W_{80} is observed only perpendicularly to the ionization axis can be interpreted as due to the fact that the outflow or jet is launched at an angle to the galaxy plane, and does not have much gas to compress along its path, only at its base in the galaxy plane. In the cases of Mrk 607 and NGC 3081, we also observe an increase in W_{80} perpendicularly to the ionization axis, but it does not reach the 600 km s^{-1} threshold for its feedback to be considered as significant. Interestingly, an enhancement in the velocity dispersion perpendicular to the ionisation axis and to a low

Downloaded from https://academic.oup.com/mnras/article/507/1/74/6324028 by Universidade Federal do Rio Grande do Sul user on 15 October 2021

Table 4. Outflow rate, power and bolometric luminosity – Columns are: (1) name of the galaxy; (2 and 5) distance in the plane of the sky from the galactic centre to the last spaxel identified as outflow dominated; (3 and 6) mass outflow rates; (4 and 7) outflow kinetic power; (8) outflow position angle; (9) AGN bolometric luminosity.

Galaxy	R_{max} [N II] (pc)	log $\dot{M}$ [N II] ($M_\odot$ yr^{-1})	log $\dot{E}$ [N II] (erg s^{-1})	R_{max} [O III] (pc)	log $\dot{M}$ [O III] ($M_\odot$ yr^{-1})	log $\dot{E}$ [O III] (erg s^{-1})	Outflow PA (°)	log L_{AGN} (erg s^{-1})
Mrk 348				158	−2.64	38.15	19	44.08
NGC 1068	171	0.30	41.38	171	0.32	41.58	30	42.85
Mrk 1058							44	
Mrk 607†							45	43.42
NGC 1365							118	43.48
NGC 1358							120	42.05
NGC 1386†	140	−2.18	38.68				110	40.89
NGC 1566								41.92
NGC 1667	235	−2.09	38.45				164	41.14
NGC 2110	336	−1.05	39.43				54	45.11
Mrk 6†	1217	2.35	43.03	1217	2.38	43.22	0	45.19
Mrk 79†				1068	−1.38	39.46	10	44.98
NGC 2787	30	−3.91	36.22				158	41.56
MCG -05-23-016								44.99
NGC 3081							0	44.22
NGC 3227	352	−2.33	37.73	269	−2.40	37.63	27	43.91
NGC 3516	501	−2.82	38.26	577	−3.00	37.03	15	44.58
NGC 3783								44.81
NGC 3786								43.70
NGC 3982								40.86
NGC 4180	115	−3.43	37.36					43.57
NGC 4450								41.04
NGC 4501							45	40.57
NGC 4593								44.01
MCG -06-30-015								44.20
NGC 5728	238	−2.07	38.06	333	−2.09	37.92	135	44.02
NGC 5899†	202	−1.67	39.07	245	−1.93	38.74	0	43.84
NGC 6300							26	43.43
NGC 6814							151	43.72
NGC 7213								43.43

Note. † indicates galaxies with equatorial outflow.

power radio jet has been reported by Venturi et al. (2021), who also argue that such characteristic is likely due to interaction between the jet and the material in the disc.

In three cases – NGC 1667, NGC 2787, and NGC 4180 – W_{80} $\geq$600 km s^{-1} is observed in a small patch close to the nucleus, bringing the total number of galaxies for which we have evaluated the feedback power of the outflows to 13 of the 30 galaxies of our sample.

In all the cases for which $W_{80} \geq 600$ km s^{-1}, we suggest that the increase in W_{80} traces mechanical feedback from the AGN, justifying its use in the quantification of the power of the outflow. In support to this interpretation we find also a notable correspondence between regions of high W_{80} and high density, which will be further discussed in Section 6.

We find additional signatures of outflows with $W_{80} \leq 600$ km s^{-1} in NGC 1365 and NGC 4593, bringing the total number of galaxies with signatures of outflows but with $W_{80} \leq 600$ km s^{-1} to 7. Thus, considering all signatures of outflows, we find them in 21 of the 30 galaxies of our sample.

5.3 Determining the ionization axis

The ionization axes were determined from the flux maps of the [N II] and [O III] lines. In order to quantify the orientation in an objective manner, we developed a method that searches for peaks in the flux map in polar coordinates. An example of this method, applied on the galaxy NGC 1386, is shown in Fig. 6.

First the image is transformed to polar coordinates based on a given centre position, and bins of angle and radius. We then have, for each radius, a separate flux as a function of the angle, which are represented by the lines in Fig. 6. Best results were achieved by using 72 bins in angle, and a step in radii of 3 pixels (0.27 arcsec), with further smoothing by convolution with a Gaussian kernel. After that each curve was normalized with respect to its maximum value. A final step, essential to avoid artificial border effects, was repeating the curves once in each angular direction, effectively wrapping the plot, and guaranteeing that pixel at 0° matches the pixel at 360°. Fig. 7 shows the resulting curves for the [N II] flux map of NGC 1386 shown in Fig. 6.

The peaks in flux for each radius are identified[2] by selecting those points which have lower values on either side, that are at a minimum distance of 120° from another peak, and that have a prominence of at least 0.3. This prominence is the difference between the height of the peak in question and the lowest point between this peak and its closest neighbour. After the direction of the peak in emission is identified for each radius, the general direction of the ionization axis is determined by a weighted mean, where the weight is the

[2]We have used the FIND_PEAKS function of the SCIPY package to implement the peak finding method.

Downloaded from https://academic.oup.com/mnras/article/507/1/74/6324028 by Universidade Federal do Rio Grande do Sul user on 15 October 2021

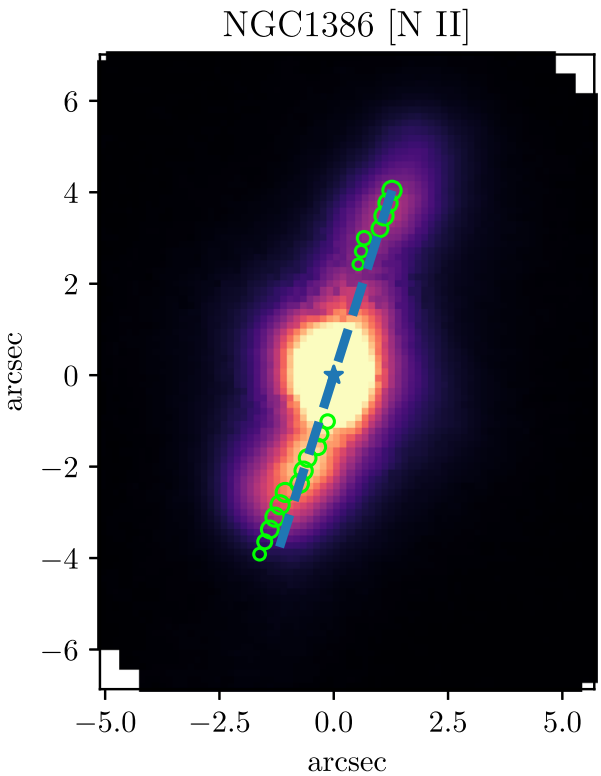

Figure 6. Example of the method for determining the ionization axis. The image is an [N II] flux map for the galaxy NGC 1386. Green circles mark peak positions, with their sizes representing the prominence of that peak. A blue star marks the centre of the galaxy, and the ionization axis is shown as the blue dashed line.

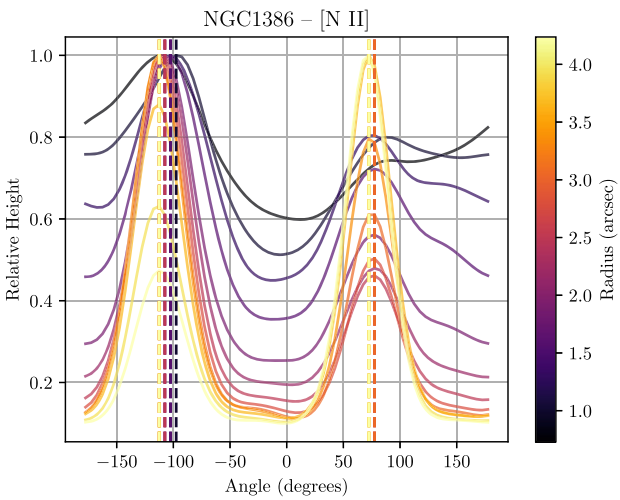

Figure 7. Relative flux map in polar coordinates for various radii, based on the image shown in Fig. 6. Each line represents a radius, identified by the colour shown in the vertical bar to the right. Vertical dashed lines mark the peak positions. The angle in the horizontal axis is measured counter-clockwise from a line extending from the centre to the right in the frame of the image.

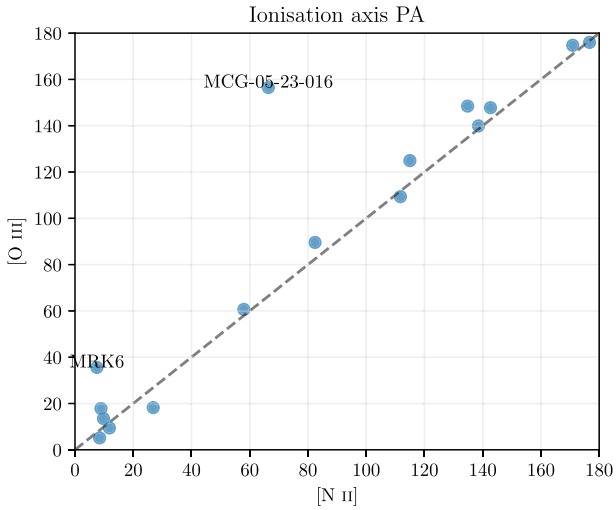

Figure 8. Comparison between the ionization axis for the [N II] and [O III] lines. There is a general agreement between the two, with only two galaxies differing by more than 15°. Only the 16 galaxies with spectral coverage reaching down to the [O III] 5007 Å line are shown here, although we have measured the [N II] ionization axis for the whole sample.

product between the distance from the centre of the galaxy and the prominence (see above) of the peak.

This method for determining the ionization axis has two main advantages: it is objective, although a little complicated at first, and it is not limited to a particular configuration of the emission profile. Fitting ellipses to isophotes, for instance, is challenging if the emission is one sided, or if it is dominated by a spiral structure.

6 DISCUSSION

6.1 Ionization and kinematic axes

Fig 8 shows the correlation between the ionization axis PA based on the emission of [N II] versus [O III] (see Section 5.3). It is clear that there is a very good agreement between the two, which is to be expected, since the flux intensity of both lines is following the same ionized structure. There are only two galaxies that differ by a reasonable amount from this direct correspondence: MCG -05-23-016 and Mrk 6, and they both have almost circular emission profiles, which reduces their significance.

The direction of the ionization axis is a tracer of the orientation of the AGN's central engine, being perpendicular to the plane of the accretion disc and the dusty torus. Some previous studies have shown that there is no relation between the orientation of the ionization axis and that of the plane of the galaxy (Schmitt et al. 2003a), although others argue for a preferable orientation of the AGN axis perpendicular to the galaxy plane, which would mean that the AGN plane would be preferably aligned with the galaxy plane (He et al. 2018). Here we use the orientation of the photometric major axis PMA (Table 3) as an indicator of the orientation of the galaxy plane. If the AGN's plane is aligned with the disc of the host galaxy, then the ionization axis should preferentially be found in a direction perpendicular to the PMA, otherwise there should be not preferred relative orientation between the two.

We investigate this possibility in Fig. 9, which is an histogram of the modulus of the difference between the PMA and the ionization axis, for both [N II] and [O III] emission lines. The results are

Downloaded from https://academic.oup.com/mnras/article/507/1/74/6324028 by Universidade Federal do Rio Grande do Sul user on 15 October 2021

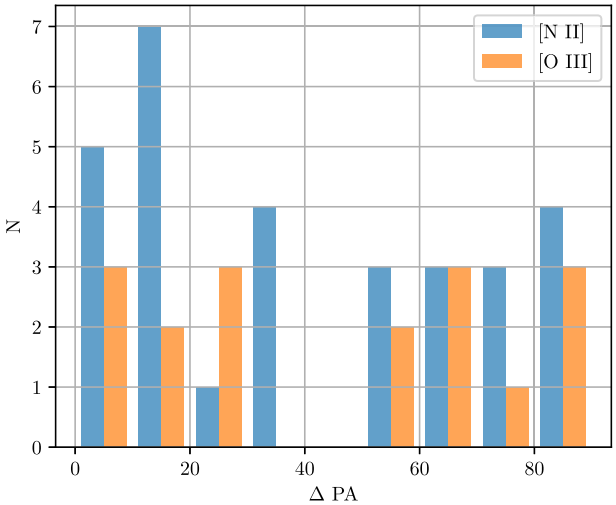

Figure 9. Histogram of the difference between the photometric major axis position angle and the orientation of the ionization axis. If there was an alignment between the plane of the AGN and that of the host galaxy's disc, there should be a concentration at high values of ΔPA. Both distributions, either considering the [N II] or [O III] emission, are indistinguishable from an uniform distribution (p-value > 0.3).

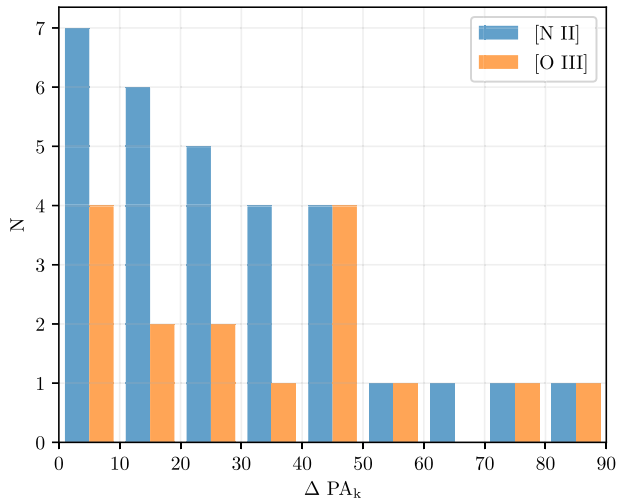

Figure 10. Difference between the orientation of the photometric major axis PMA and the gas kinematic major axes [O III] and [N II] KMA at the central kiloparsec (Table 3) Since the PMA admits two rotation directions, the differences shown here are restricted to 90°. Blue bars represent ΔPA_k for the [N II] velocity field, while orange bars refer to the [O III] velocity field.

compatible with there being no preferential orientation of the AGN with respect to the disc of the host galaxy. A Kolmogorov–Smirnov (KS) test comparing the measured distribution of ΔPA against a uniform distribution with the same dispersion returns p-values >0.3, meaning that the current sample is statistically indistinguishable from random orientations for the ionization axis relative to the galaxy plane.

The PMA is also a good proxy for the orientation of the large-scale kinematics of the host galaxy (dominated by rotation in the galaxy plane), since all of our targets are disc galaxies. By comparing the orientation of the velocity fields probed by our measurements with that of the PMA we can assess the misalignment between the ionized gas kinematics within the FoV of our measurements with that of the large-scale kinematics of the galaxy. In order to investigate this, we present in Fig. 10 two histograms, showing the difference between the orientations of the kinematic major axes KMA of [N II] and [O III] velocity fields (Table 3) and that of the PMA. We note that the PMA is the same for two rotation directions, causing this analysis to be restricted to a misalignment of 90° or less; if a source has $\Delta PA_k = 180°$ it would show as $\Delta PA_k = 0$, but we have only one such case in our sample, Mrk 607 (Freitas et al. 2018).

The analysis of Fig. 10 reveals that, for the [N II] velocity field, there is a concentration towards low values of ΔPA_k, meaning that for most sources the [N II] velocity field is dominated by co-planar rotation with the galactic disc. But, when considering the [O III] velocity field, the distribution of ΔPA_k is skewed towards higher values, which we interpret as a consequence of its closer connection with the AGN outflow that is oriented at random directions relative to the galaxy plane, as discussed above.

6.2 AGN bolometric luminosities

In order to relate the AGN properties with its total luminosity, we have estimated the bolometric luminosities from X-Ray fluxes in the 14–195 keV band when available, and from the 2–10 keV band otherwise. Conversion between X-Ray luminosity and bolometric luminosity follows band specific correction formulae, both based on Marconi et al. (2004). For the 2–10 keV band specifically, we used equation (21) from Marconi et al. (2004):

$$\log\left[\frac{L_{12}}{L_{2-10\ \mathrm{keV}}}\right] = 1.54 + 0.24L_{12} + 0.012L_{12}^2 - 0.0015L_{12}^3, \quad (2)$$

where $L_{12} = \log(L_{AGN}) - 12$ and L_{AGN} is the bolometric luminosity in units of $L_\odot$. However, for the majority of targets the 14-195 keV flux from the *Swift*-BAT survey was available, and the bolometric correction followed equation (5) from Ichikawa et al. (2017):

$$L_{AGN} = 0.0378(\log L_{14-195\ \mathrm{keV}})^2 - 2.03\log L_{14-195\ \mathrm{keV}} + 61.6, \quad (3)$$

The bolometric luminosities obtained using the above two equations are listed in the last column of Table 4.

6.3 Gas kinematics

For the remainder of this section we adopt the hypothesis that the signature of mechanical feedback of outflows on to the surrounding medium is an increase in W_{80}, and from there we calculate the associated mass-outflow rates and kinetic powers. This analysis based on general criteria differs from the one presented in Section 5, where we discussed outflows considering more aspects of the velocity field.

In order to quantify the outflows, we need to identify the spaxels in which the ionized gas kinematics is not compatible with disc rotation. A spaxel is defined as being part of an outflow, or having its nebular emission dominated by outflowing gas according to the following criteria:

(i) It has $W_\lambda(\mathrm{H}\alpha) > 6$ Å to ensure an accurate value for $L_{\mathrm{H}\alpha}$. Keeping in mind that, in a fraction of galaxies, the stellar spectrum has not been subtracted, this limit in $W_\lambda(\mathrm{H}\alpha)$ means that the Hα emission typically has $W_\lambda(\mathrm{H}\alpha) \geq 9$ Å, since the $W_\lambda(\mathrm{H}\alpha)$ associated with the absorption is expected to be close to 3 Å.

(ii) The velocity dispersion measured by W_{80} of the [O III] or [N II] emission lines must be above a limit which excludes reasonable expectations for bound orbits in the galaxy's potential. For this limit we chose $W_{80} > 600$ km s^{-1}.

Downloaded from https://academic.oup.com/mnras/article/507/1/74/6324028 by Universidade Federal do Rio Grande do Sul user on 15 October 2021

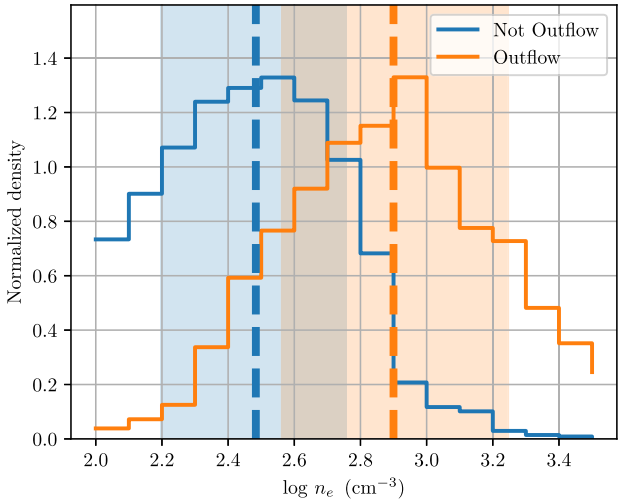

Figure 11. Histograms of electron density for spectra from spaxels covering (orange) and not covering (blue) outflows, in units of probability density. Median values are shown as vertical dashed lines, and the shaded regions encompass the 16 and 84 percentiles.

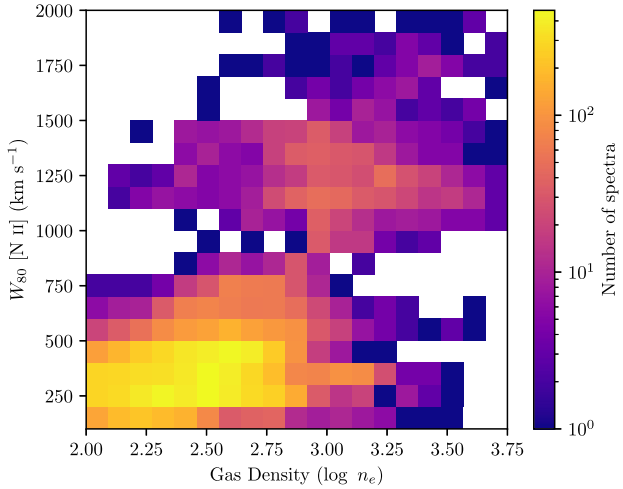

Figure 12. Comparison between the density and the [N II] W_{80}. Each axis has been divided into 20 cells and colour coded according to the number of points in each cell, totalling ∼1.4 × 10^4 individual spectra (see the text).

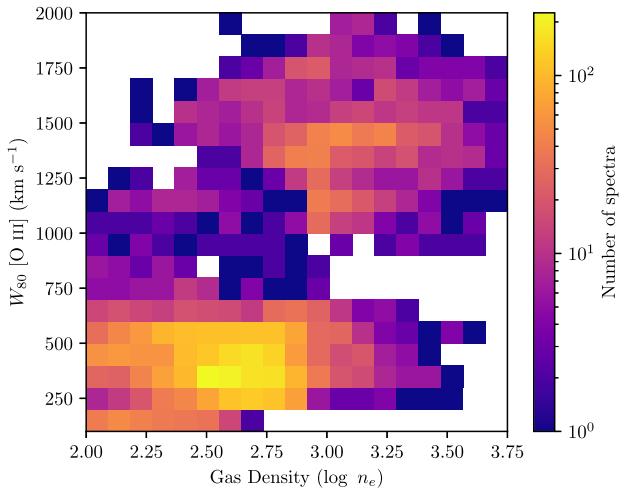

Figure 13. Analogous to Fig. 12 but for the [O III] line.

Although the [O III] 5007 Å line is a better proxy for the gas ionized by radiation from the AGN, we decided to include also measurements using the [N II] line to avoid limiting the size of our sample to those for which such measurements could be made.

(iii) It has at least two more neighbouring spaxels also classified as having outflows. This last criterion ensures that isolated spurious spaxels are not included in the outflow mask. Since the FWHM of the point spread function typically spans three to six spaxels, isolated detections must be false positives.

Using these simple and very general criteria, we reach the conclusion that 13 out of the 30 AGNs in our sample display signatures of outflows in ionized gas via W_{80}. These galaxies can be identified in Table 4 as those for which we show the mass outflow rates $\dot{M}$ and outflow powers $\dot{E}$.

6.4 Gas densities in the outflows

We have used the [S II] lines λλ6716, 6731 Å to estimate the electron density at each spaxel of our sample galaxies. The actual computation followed the equations of Proxauf, Öttl & Kimeswenger (2014). The only galaxies for which we do not show electron density estimates are NGC 3227 and NGC 3786 due to an observational problem that precluded the use of the [S II] lines. For all spectra we adopted a fixed standard electron temperature of 10^4 K. If temperatures in the outflows were higher, this would increase the estimated densities.

Fig. 11 shows the histogram of electron densities for spectra identified as having outflows (corresponding to spaxels with W_{80} ≥600 km s^{-1}) as compared to those without outflows. The histograms are given in units of probability density, which means that the integral of the histogram equals 1. Median values are 305^{+266}_{-147} cm^{-3} and 794^{+969}_{-429} cm^{-3} for the non-outflow and outflow samples respectively, where the given intervals are the distances from the median to the 16 and 84 percentiles. These density values are in reasonable agreement with recent results based on nine Seyfert galaxies observed with MUSE (Mingozzi et al. 2019). Spectra for which only upper or lower limits could be given, due to the saturation of the line ratio, are not included in these statistics. The numbers of sample points are 14 604 and 2110 for non-outflows and outflows, respectively.

We performed a KS test in order to ascertain the statistical significance of the difference in distributions of electron densities, arriving at a value $D = 0.51$ (a value of 0 indicates that both distributions are drawn from the same sample). Given the large size of this sample of spectra, we can confirm the rejection of the null hypothesis with a confidence, given by the p-value, of $p < 0.1$ per cent. Therefore we conclude that the gas in outflow is on average denser than the rest of the narrow-line region, by a factor of 1.7. This result supports that the criteria listed in Section 6 are indeed selecting a physically distinct portion of the emitting gas.

This same effect can also be seen in plots comparing the electron density to the W_{80} for each spectrum, which are shown in Figs 12 and 13. Only spectra satisfying the following conditions were used in these figures: (i) SNR in the [S II] lines above 3; (ii) no bad pixel flags compromising the accuracy of W_{80} in the [N II] or [O III] lines; (iii) [S II] unaffected by strong telluric lines. Adoption of these criteria reduced the number of points to about 1.4 × 10^4, which represent roughly 10 per cent of all the spectra in the sample. The two regimes

Downloaded from https://academic.oup.com/mnras/article/507/1/74/6324028 by Universidade Federal do Rio Grande do Sul user on 15 October 2021

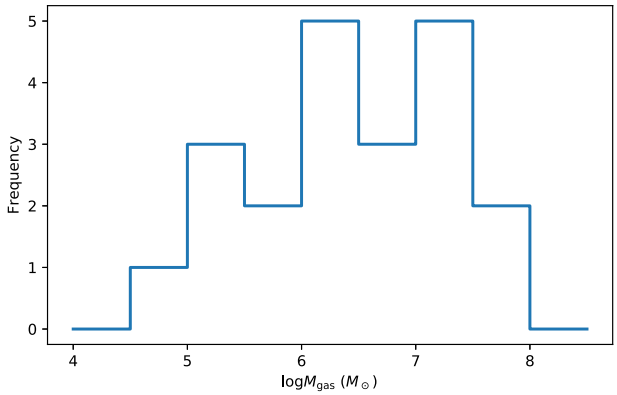

Figure 14. Histogram of ionized gas mass of galaxies in the sample (within the IFU's field of view), based on the Hα luminosity and the gas density derived from the [S II] line ratio.

identified in the histogram (Fig. 11) are now seen as two clouds: one having W_{80} ~400 km s^{-1} and low densities, and the other with W_{80} above 800 km s^{-1} and higher densities.

Our interpretation of this connection between velocity dispersion and electron density is that the gas which forms the outflow is encountering the galaxy's interstellar medium (ISM) and increasing the local density. Of course, this interpretation requires the outflow to be directed along a direction which meets the disc of the galaxy. Outflows perpendicular to the galaxy's disc would, therefore, produce a comparatively smaller effect on the density. Another possibility could be that the outflowing gas is being spread out in the direction of the line of sight, hence the increase in W_{80}, when it meets regions of higher density in the ISM. Both interpretations differ in the cause attributed to the increased W_{80}, which is intrinsic to the outflow in the first, and a consequence of higher density clouds in the second.

6.5 Ionized gas mass

The ionized gas mass was calculated for each individual spaxel of each galaxy as

$$M = \frac{m_p L_{\mathrm{H}\alpha}}{n_e j_{\mathrm{H}\alpha}(T)} \tag{4}$$

where m_p is the proton mass, n_e is the number density of electrons from the [S II] lines flux ratio, $L_{\mathrm{H}\alpha}$ is the Hα luminosity, and $j_{\mathrm{H}\alpha}$ is the Hα emissivity in erg cm^3 s^{-1} for a given temperature.

Since we did not measure the temperature based on the nebular emission, we assume a standard value for the electron temperature of $T = 10^4$ K. The Hα luminosity was corrected only for foreground Galactic extinction based on the CCM (Cardelli, Clayton & Mathis 1989) extinction law, using the dust maps from IRSA (Schlegel, Finkbeiner & Davis 1998). A factor of $10^{0.4A}$ was applied to the measured flux, where A is the extinction in magnitudes for the SDSS r' band. We did not correct for extinction within the galaxy due to the fact that we do not have suitable Hβ fluxes or other reddening indicators to obtain the internal attenuation. A histogram of the total ionized gas masses for our sample, obtained by summing the masses evaluated at each spaxel within the observed FoV, is shown in Fig. 14.

6.6 Mass outflow rates

In order to calculate the mass outflow rates we have used the Hα luminosity. However, instead of using the total flux of Hα emission, we used only the fraction of the flux which corresponds to velocities above 600 km s^{-1} from the line centre. This ensures that even if the W_{80} of Hα is different from that of [O III], only the emission from the outflowing gas is considered.

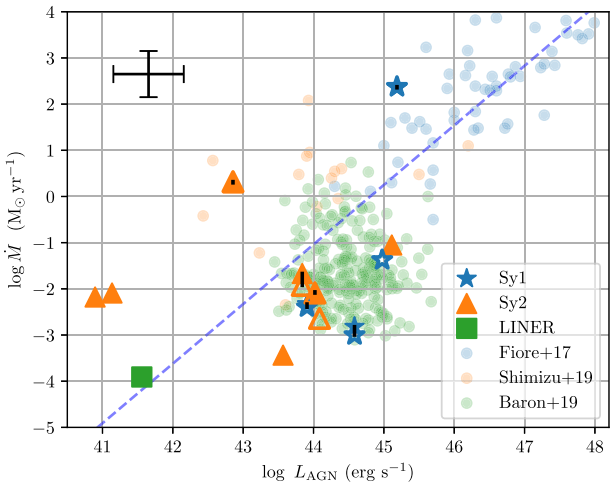

Figure 15. Relation between the mass outflow rate $\dot{M}$ and the AGN's bolometric luminosity L_{AGN}. Stars, triangles, and squares represent Sy 1, Sy 2, and LINERs, respectively. Filled symbols are for outflow rates based on the [N II] line, while open symbols are based on [O III]. When estimates based on both [O III] and [N II] are available, the symbols are joined by a vertical black line. Blue circles are from Fiore et al. (2017), orange circles from Shimizu et al. (2019), and green circles from Baron & Netzer (2019). The blue dashed line is the sublinear fit of Fiore et al. (2017). Typical uncertainties are represented by the black cross at the upper left. When an outflow is detected in both [N II] and [O III], the symbols are linked by a vertical black line.

Mass outflow rates are given by equation (5) below. The basic assumption is that the outflow velocity v we see now is approximately the average velocity of the gas since it left the vicinity of the AGN. Therefore, the time it took for the gas to reach its current distance from the central engine is R/v:

$$\dot{M} = M\frac{v}{R}, \tag{5}$$

where we have adopted 1/2 W_{80} as a proxy for the outflow velocity, which should be a good approximation when considering many galaxies, and therefore, many different projections for the outflow. The resulting mass outflow rate values for each galaxy, as derived from the kinematics of both the [O III] and [N II] emission lines, are given in Table 4.

By far the most uncertain term in equation (5) is the distance R. Even before any projection effects are taken into account, one first has to consider where the gas is being accelerated, either at the vicinity of the AGN or *in situ* (i.e. Kraemer et al. 2020, and references therein). In this work we adopt a model of outflow in the form of an expanding spherical shell, which we assume to be accelerated at the nucleus. We define the outflow travel distance R as the largest radius, in the plane of the sky, for which we observe $W_{80} \geq 600$ km s^{-1}. This is, of course, a lower limit for the travel distance in the likely case that the outflows are not spherically symmetric. As a result, our estimates of mass outflow rates should be considered as upper limits.

In Fig. 15, we show the relation between the mass outflow rates $\dot{M}$ and the AGN bolometric luminosity L_{AGN} for the 13 galaxies of our sample with outflows as traced by $W_{80} \geq 600$ km s^{-1} together with previous results from the literature. Spectral types Sy 1 and Sy 2 and LINERs are represented by different symbols in the figure, although we are not implying any distinction in the outflow mechanism. In this

Downloaded from https://academic.oup.com/mnras/article/507/1/74/6324028 by Universidade Federal do Rio Grande do Sul user on 15 October 2021

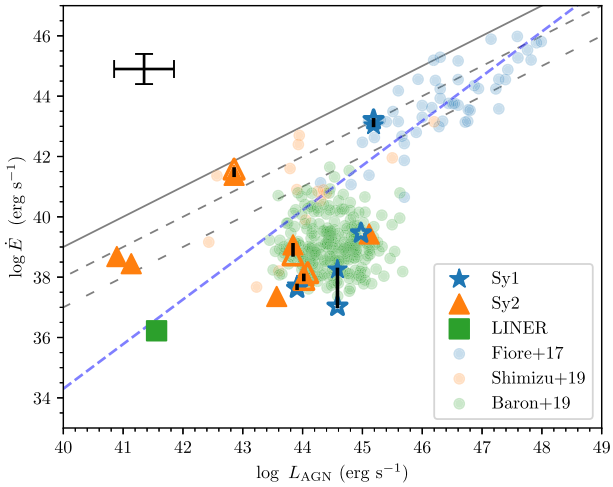

Figure 16. Relation between the outflow power $\dot{E}$ and the AGN bolometric luminosity $L_{\rm AGN}$ for our galaxies compared to previous value from the literature. The dashed blue line shows the sublinear fit from Fiore et al. (2017). Continuous and dashed grey lines are a visual aid representing outflow powers, from top to bottom, of 0.1 $L_{\rm AGN}$, 0.01 $L_{\rm AGN}$, and 0.001 $L_{\rm AGN}$, respectively. Distinct AGN spectral types are represented by different symbols. Filled symbols represent values based on the [N II] line while open symbols represent values based on the [O III] line.

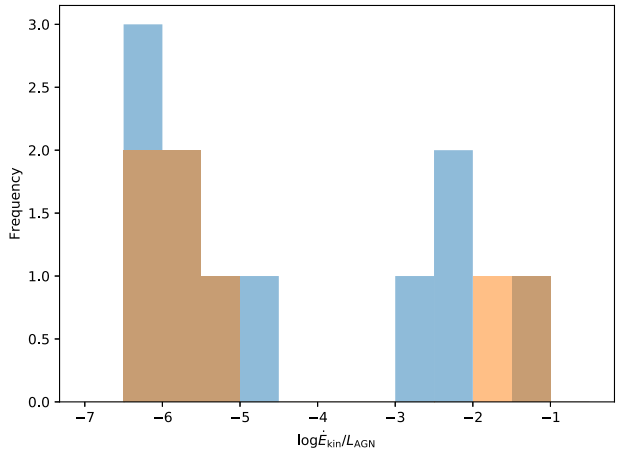

Figure 17. Histogram of the ratios between the outflow power $\dot{E}$ and the AGN bolometric luminosity $L_{\rm AGN}$. Blue bars are for estimates based on [N II] and orange bars are based on [O III].

plot we see that the values obtained for our galaxies follow the trend of the sublinear correlation with $L_{\rm AGN}$ from Fiore et al. (2017) – the blue dashed line in the figure. The scatter is nevertheless large, with four points two orders of magnitude above the mean relation, one on the relation and the rest of the sample 1–2 orders of magnitude below the relation. Most of the points below the relation occupy the same space as those from Baron & Netzer (2019). We have also added points compiled by Shimizu et al. (2019) for reference. Some of our galaxies are also present in these references, therefore the same galaxy might be represented by more than one point.

When comparing the galaxies with and without outflows a small trend is also observed, although the luminosities are consistent within uncertainties. For the 13 galaxies with outflows the average AGN luminosity is log $L_{\rm AGN}$ of 43.83 ± 0.83, while for galaxies lacking outflows the average value is log $L_{\rm AGN}$ is 42.94 ± 1.54.

6.7 Outflow power

Having the mass outflow rate, estimating the outflow power is relatively straightforward. We consider only the mechanical power of the outflow, disregarding eventual heating and expansion of the outflowing gas. The total kinetic power of the outflow is given by

$$P = \frac{1}{2}\dot{M}v^2 \tag{6}$$

where v is the outflow velocity, taken to be 1/2 W_{80} for W_{80} higher than 600 km s^{-1}. The calculated values are shown in the fourth and seventh columns of Table 4, and range between $10^{36.2}$ erg s^{-1} for the LINER in NGC 2787 and $10^{43.3}$ erg s^{-1} for the Sy 1 in Mrk 6, with a median value of $\log[\dot{E}/(\mathrm{erg\,s^{-1}})] = 38.5^{+1.8}_{-0.9}$ when considering [N II] based W_{80}. Similar results are found for [O III] based estimates, with a median outflow power of $\log[\dot{E}/(\mathrm{erg\,s^{-1}})] = 38.4^{+2.9}_{-0.8}$.

Fig. 16 shows the relation between the outflow kinetic power $\dot{E}$ and the AGN luminosity $L_{\rm AGN}$ as compared with previous ones from the literature in the reference plot of Fiore et al. (2017). The blue dashed line in the figure shows the sublinear correlation from Fiore et al. (2017) for ionized gas outflows.

Previous models and studies have argued that the relation between the kinetic power and the AGN luminosity should be $0.05L_{\rm AGN} \geq \dot{E} \geq 0.5L_{\rm AGN}$ for a significant impact of the AGN on the evolution of the host galaxy (Di Matteo, Springel & Hernquist 2005; Hopkins & Quataert 2010; Zubovas & King 2012). As a reminder, we are only addressing one manifestation of outflow – the ionized gas phase – which is linked to radiation pressure driven winds. Fig. 16 and the histogram of the ratios $\dot{E}/L_{\rm AGN}$ shown in Fig. 17 reveal that only for two galaxies of our sample – NGC 1068 and Mrk 6 – the outflows have such power. The remaining outflows have powers below $10^{-2}\,L_{\rm AGN}$. When compared to previous results from the literature, our four most powerful outflows follow the trend of the higher luminosity sources of Fiore et al. (2017) and Shimizu et al. (2019), while the other sources are much less powerful, showing a behaviour more similar to the lower-luminosity sources of Baron & Netzer (2019).

7 CONCLUSIONS

We present an analysis of GMOS-IFU optical data cubes of the inner kpc of 30 nearby AGN (mostly at $z \leq 0.01$) that our research group AGNIFS has collected over the years, and have measured the gas excitation and kinematics via the fit of Gauss–Hermite polynomials to the emission lines. We have obtained maps of the gas emission-line flux distributions, line ratios, and kinematics with spatial resolutions in the range 50–300 pc and velocity resolution of ≈50 km s^{-1} and used the parameter W_{80} as an indicator of outflows. A total of 21 of the 30 galaxies of our sample are *Swift*/BAT AGN sources. We determined the orientation of the ionization axis by finding the direction of the peak fluxes in the polar flux distributions of [N II] and [O III]. We fitted the [N II] and [O III] velocity fields with a simple symmetric model to measure the gaseous systemic velocities, the PA of the corresponding kinematic major axes, and to reveal the presence of outflows.

The main conclusions we have reached on the basis of the measurements outlined above are:

(i) *Gas excitation and ionization axis:* Emission-line ratios characteristic of AGN excitation are observed over most of the FoV and the gas emission clearly extends beyond the inner kpc; the ionization

Downloaded from https://academic.oup.com/mnras/article/507/1/74/6324028 by Universidade Federal do Rio Grande do Sul user on 15 October 2021

axis shows a random orientation relative to the photometric major axis of the galaxy indicating no preferred orientation of the AGN relative to the galaxy;

(ii) *Gas kinematics:* Disc rotation is found in most cases, as expected given the spiral morphology of the host galaxies, though disturbances due to inflows and outflows are also seen. The gas velocity dispersion and W_{80} are usually enhanced at the nucleus and/or surrounding outflows, where the highest gas densities are frequently also seen;

(iii) *Outflows:* Outflows have been found in 21 sources. Most of them are oriented along the ionization axis and associated with an increase in the W_{80}. In 7 sources, increased W_{80} values occur in a band crossing the nucleus perpendicularly to the ionization axis which we attribute to the passage of an outflow or radio jet pushing the ambient gas sideways. Of the 21 sources with outflows, only 13 show $W_{80} \geq 600$ km s^{-1}; mass outflow rates and powers are only calculated for the latter;

(iv) *Impact of outflows via* W_{80}: We have employed the W_{80} index as an indicator of outflows, using a lower limit of 600 km s^{-1} to isolate regions dominated by outflows (as lower profile widths can be associated to rotation). We find such signature in 13 of the 30 AGNs of our sample. Seven additional galaxies show other signatures of outflows, although presenting $W_{80} < 600$ km s^{-1}; we attribute these low values to the fact that such outflows have a low impact on the surrounding gas;

(v) *Gas densities* n_e *in the outflows:* We found that the gas densities – determined via the [S II] line ratio – tend to be higher in the regions with outflows ($W_{80} \geq 600$ km s^{-1}) than in those without, with median values of $n_e \approx 800$ cm^{-3} and $n_e \approx 300$ cm^{-3}, respectively;

(vi) *Ionized gas mass within the inner kpc:* Total ionized gas masses within the $\approx$ inner kiloparsec are in the range $10^{4.5}$–10^{8} M$_\odot$;

(vii) *Mass outflow rate* $\dot{M}$*:* Using W_{80} as a proxy for the outflow gas velocity $v = 1/2\, W_{80}$ and a distance of the outflow corresponding to the largest observed radial distance from the nucleus at which $W_{80} \geq 600$ km s^{-1}, we obtain mass outflow rates in the range $\log[\dot{M}/(\mathrm{M}_\odot\,\mathrm{yr}^{-1})] = -3.91$ to $\log[\dot{M}/(\mathrm{M}_\odot\,\mathrm{yr}^{-1})] = 2.38$, with a median value of $\log[\dot{M}/(\mathrm{M}_\odot\,\mathrm{yr}^{-1})] = -2.1^{+1.6}_{-1.0}$, where the upper and lower limits represent the 16 and 84 percentiles.

(viii) *Outflow power* $\dot{E}$*:* Outflow powers are in the range $\sim 10^{37}$ erg s^{-1} to $\sim 10^{43}$ erg s^{-1}. When compared to the AGN bolometric luminosities $L_{\rm AGN}$, $\log(\dot{E}) \geq 0.01\, L_{\rm AGN}$ only for 2 sources, for two others $0.001 \geq \log(\dot{E})/L_{\rm AGN} \geq 0.01$, while for the remainder 10 galaxies, the powers are lower than $0.001\, L_{\rm AGN}$.

(ix) *Relation* $\dot{M}$ *versus* $L_{\rm AGN}$: The mass outflow rate shows some correlation with $L_{\rm AGN}$, with a large scatter; when compared to the previous results from the literature (e.g. Fiore et al. 2017), they seem to approximately follow the same relation, on average, with three points above, one on the relation and most of them below the relation;

(x) *Relation* $\dot{E}$ *versus* $L_{\rm AGN}$: There is also some correlation between the outflow powers and $L_{\rm AGN}$, also with a large scatter; when added to the previous relation of Fiore et al. (2017), the four most powerful outflows in our sample follow the trend of the being in the range $0.001\, L_{\rm AGN} \geq \log(\dot{E}) \geq 0.1\, L_{\rm AGN}$, while the outflows in the remaining galaxies of our sample populate a region well below the previous relation.

ACKNOWLEDGEMENTS

TSB would like to thank the Gemini Brazilian National Time Allocation Committee (NTAC), the International Time Allocation Committee (ITAC), and the Gemini Observatory for the support to all these observations, collected over approximately 10 yr. TSB would like to thank as well all the Institutes where the proposals and the analyses of the observations have been carried out: Instituto de Física, Universidade Federal do Rio Grande do Sul, Universidade Federal de Santa Catarina, Universidade Federal de Santa Maria, Rochester Institute of Technology, and Harvard-Smithsonian Center for Astrophysics, as well as CAPES, CNPq, and FAPERGS for financial support. DRD would like to thank CAPES and CNPq for financial support during this research. RAR thanks partial financial support from Conselho Nacional de Desenvolvimento Científico e Tecnológico (202582/2018-3 and 302280/2019-7) and Fundação de Amparo à Pesquisa do Estado do Rio Grande do Sul (17/2551-0001144-9 and 16/2551-0000251-7). NN acknowledges support from CONICYT (PIA ACT172033, Fondecyt 1171506, and BASAL AFB-170002). This work was supported in part by the National Science Foundation under Grant No. AST-1108786.

Based on observations obtained at the Gemini Observatory, which is operated by the Association of Universities for Research in Astronomy, Inc., under a cooperative agreement with the NSF on behalf of the Gemini partnership: the National Science Foundation (United States), National Research Council (Canada), CONICYT (Chile), Ministerio de Ciencia, Tecnología e Innovación Productiva (Argentina), Ministério da Ciência, Tecnologia e Inovação (Brazil), and Korea Astronomy and Space Science Institute (Republic of Korea).

DATA AVAILABILITY

The data underlying this article will be shared on reasonable request to the corresponding author. The following additional information and figures are available as online supplementary material: comments on individual galaxies (Appendix A); acquisition images with the overlaid GMOS FoV and sample spectrum (Appendix B); data plots for all galaxies (Appendix C); results of Gauss–Hermite higher order moments (Appendix D); WHAN diagnostic diagrams (Appendix E).

REFERENCES

Alexander D. M., Hickox R. C., 2012, New Astron. Rev., 56, 93
Allington-Smith J. et al., 2002, PASP, 114, 892
Barbosa F. K. B., Storchi-Bergmann T., Fernandes R. C., Winge C., Schmitt H., 2009, MNRAS, 396, 2
Baron D., Netzer H., 2019, MNRAS, 486, 4290
Bradley L. et al., 2018, astropy/photutils: v0.5. doi:10.5281/ZENODO.1340699, https://zenodo.org/record/1340699#.W3vzGxgnaV4
Brandt W. N., Alexander D. M., 2015, A&AR, 23, 1
Brum C., Riffel R. A., Storchi-Bergmann T., Robinson A., Schnorr Müller A., Lena D., 2017, MNRAS, 469, 3405
Bruzual G., Charlot S., 2003, MNRAS, 344, 1000
Cappellari M., 2017, MNRAS, 466, 798
Cappellari M., Emsellem E., 2004, PASP, 116, 138
Cardelli J. A., Clayton G. C., Mathis J. S., 1989, ApJ, 345, 245
Cicone C. et al., 2014, A&A, 562, A21
Cid Fernandes R., Stasinska G., Mateus A., Vale Asari V., 2010, MNRAS, 413, 1687
Combes F. et al., 2014, A&A, 565, A97
Dall'Agnol de Oliveira B. et al., 2021, MNRAS, 504, 3890
Davies R. L. et al., 2020, ApJ, 894, 28
Di Matteo T., Springel V., Hernquist L., 2005, Nature, 433, 604
Diniz M. R., Riffel R. A., Storchi-Bergmann T., Winge C., 2015, MNRAS, 453, 1727
Drake C. L., McGregor P. J., Dopita M. A., van Breugel W. J. M., 2003, AJ, 126, 2237

Downloaded from https://academic.oup.com/mnras/article/507/1/74/6324028 by Universidade Federal do Rio Grande do Sul user on 15 October 2021

Erwin P., 2004, A&A, 415, 941
Fabian A., 2012, ARA&A, 50, 455
Falcón-Barroso J., Sánchez-Blázquez P., Vazdekis A., Ricciardelli E., Cardiel N., Cenarro A. J., Gorgas J., Peletier R. F., 2011, A&A, 532, A95
Fathi K., Storchi-Bergmann T., Riffel R. A., Winge C., Axon D. J., Robinson A., Capetti A., Marconi A., 2006, ApJ, 641, L25
Ferrarese L., Merritt D., 2000, ApJ, 539, L9
Fiore F. et al., 2017, A&A, 601, A143
Freitas I. C. et al., 2018, MNRAS, 476, 2760
Gebhardt K. et al., 2000, ApJ, 539, L13
Gültekin K. et al., 2009, ApJ, 698, 198
Harrison C. M. et al., 2012, ApJ, 760, L15
Harrison C. M., 2017, Nat. Astron., 1, 0165
Harrison C., 2014, PhD thesis, Durham University
He Z. et al., 2018, MNRAS, 478, 3614
Herrera-Camus R. et al., 2019, ApJ, 871, 37
Hickox R. C., Mullaney J. R., Alexander D. M., Chen C.-T. J., Civano F. M., Goulding A. D., Hainline K. N., 2014, ApJ, 782, 9
Hinshaw G. et al., 2012, ApJS, 208, 25
Hopkins P. F., Quataert E., 2010, MNRAS, 407, 1529
Humire P. K. et al., 2018, A&A, 614, A94
Ichikawa K., Ricci C., Ueda Y., Matsuoka K., Toba Y., Kawamuro T., Trakhtenbrot B., Koss M. J., 2017, ApJ, 835, 74
Kormendy J., Ho L. C., 2013, ARA&A, 51, 511
Kraemer S. B., Turner T. J., Couto J. D., Crenshaw D. M., Schmitt H. R., Revalski M., Fischer T. C., 2020, MNRAS, 493, 3893
Krajnovic D., Cappellari M., de Zeeuw P. T., Copin Y., 2006, MNRAS, 366, 787
Lang D., Hogg D. W., Mierle K., Blanton M., Roweis S., 2010, AJ, 139, 1782
Lena D. et al., 2015, ApJ, 806, 22
Lena D., Robinson A., Storchi-Bergmann T., Couto G. S., Schnorr-Müller A., Riffel R. A., 2016, MNRAS, 459, 4485
Leung T. K. D., Riechers D. A., Pavesi R., 2017, ApJ, 836, 180
Madau P., Dickinson M., 2014, ARA&A, 52, 415
Marconi A., Risaliti G., Gilli R., Hunt L. K., Maiolino R., Salvati M., 2004, MNRAS, 351, 169
McNamara B. R., Nulsen P. E. J., 2012, New J. Phys., 14, 55023
Mingozzi M. et al., 2019,A&A, 622,A146
Monet D. G. et al., 2003, AJ, 125, 984
Mundell C. G., James P. A., Loiseau N., Schinnerer E., Forbes D. A., 2004, ApJ, 614, 648
Muñoz-Vergara D. et al., 2019, MNRAS, 487, 3679
Noordermeer E., van der Hulst J. M., Sancisi R., Swaters R. A., van Albada T. S., 2005, A&A, 442, 137
Oh K. et al., 2018, ApJS, 235, 4
Osterbrock D. E., Ferland G. J., 2006, Astrophysics of Gaseous Nebulae and Active Galactic Nuclei, 2nd edn. University Science Books, Sausalito, California. http://adsabs.harvard.edu/abs/2006agna.book.....O
Proxauf B., Öttl S., Kimeswenger S., 2014, A&A, 561, A10
Ramasawmy J., Stevens J., Martin G., Geach J. E., 2019, MNRAS, 486, 4320
Riffel R. A. et al., 2018, MNRAS, 474, 1373
Riffel R. A., 2010, Ap&SS, 327, 239
Riffel R. A., Storchi-Bergmann T., Riffel R., Dahmer-Hahn L. G., Diniz M. R., Schönell A. J., Dametto N. Z., 2017, MNRAS, 470, 992
Riffel R. A., Storchi-Bergmann T., Winge C., 2013, MNRAS, 430, 2249
Rodighiero G. et al., 2019, ApJ, 877, L38
Rodríguez-Ardila A., Prieto M. A., Mazzalay X., Fernández-Ontiveros J. A., Luque R., Müller-Sánchez F., 2017, MNRAS, 470, 2845
Ruschel-Dutra D., Dall'Agnol de Oliveira B., 2020, danielrd6/ifscube v1.0. doi:10.5281/zenodo.3945237, https://doi.org/10.5281/zenodo.3945237
Schaye J. et al., 2015, MNRAS, 446, 521
Schlegel D. J., Finkbeiner D. P., Davis M., 1998, ApJ, 500, 525
Schmitt H. R., Donley J. L., Antonucci R. R. J., Hutchings J. B., Kinney A. L., 2003b, ApJS, 148, 327
Schmitt H. R., Donley J. L., Antonucci R. R. J., Hutchings J. B., Kinney A. L., Pringle J. E., 2003a, ApJ, 597, 768
Schmitt H. R., Ulvestad J. S., Antonucci R. R. J., Kinney A. L., 2001, ApJS, 132, 199
Schnorr-Müller A., Storchi-Bergmann T., Ferrari F., Nagar N. M., 2017a, MNRAS, 466, stx018
Schnorr-Müller A., Storchi-Bergmann T., Nagar N. M., Ferrari F., 2014a, MNRAS, 438, 3322
Schnorr-Müller A., Storchi-Bergmann T., Nagar N. M., Robinson A., Lena D., 2017b, MNRAS, 471, 3888
Schnorr-Müller A., Storchi-Bergmann T., Nagar N. M., Robinson A., Lena D., Riffel R. A., Couto G. S., 2014b, MNRAS, 437, 1708
Schnorr-Müller A., Storchi-Bergmann T., Robinson A., Lena D., Nagar N. M., 2016, MNRAS, 457, 972
Scholtz J. et al., 2018, MNRAS, 475, 1288
Schönell A. J., Storchi-Bergmann T., Riffel R. A., Riffel R., Bianchin M., Dahmer-Hahn L. G., Diniz M. R., Dametto N. Z., 2019, MNRAS, 485, 2054
Schulze A. et al., 2019, MNRAS, 488, 1180
Sharp R. G., Bland-Hawthorn J., 2010, ApJ, 711, 818
Shimizu T. T. et al., 2019, MNRAS, 490, 5860
Slater R. et al., 2019, A&A, 621, A83
Soto-Pinto P. et al., 2019, MNRAS, 489, 4111
Springel V., Di Matteo T., Hernquist L., 2005, MNRAS, 361, 776
Stanley F., Harrison C. M., Alexander D. M., Swinbank A. M., Aird J. A., Del Moro A., Hickox R. C., Mullaney J. R., 2015, MNRAS, 453, 591
Stetson P. B., 1987, PASP, 99, 191
Storchi-Bergmann T., Bonatto C. J., 1991, MNRAS, 250, 138
Storchi-Bergmann T., Dors O. L., Riffel R. A., Fathi K., Axon D. J., Robinson A., Marconi A., Ostlin G., 2007, ApJ, 670, 959
Storchi-Bergmann T., Lopes R. D. S., McGregor P. J., Riffel R. A., Beck T., Martini P., 2010, MNRAS, 402, 819
Storchi-Bergmann T., McGregor P. J., Riffel R. A., Simões Lopes R., Beck T., Dopita M., 2009, MNRAS, 394, 1148
Storchi-Bergmann T., Schnorr-Müller A., 2019, Nat. Astron., 3, 48
Sun A.-L., Greene J. E., Zakamska N. L., 2017, ApJ, 835, 222
Tully R. B. et al., 2013, AJ, 146, 25
van den Bosch R. C. E., 2016, ApJ, 831, 134
van der Marel R. P., Franx M., 1993, ApJ, 407, 525
Vayner A., Wright S. A., Murray N., Armus L., Larkin J. E., Mieda E., 2017, ApJ, 851, 126
Vazdekis A., Sánchez-Blázquez P., Falcón-Barroso J., Cenarro A. J., Beasley M. A., Cardiel N., Gorgas J., Peletier R. F., 2010, MNRAS, 404, 1639
Venturi G. et al., 2021, A&A, 628, A17
Véron-Cetty M.-P., Véron P., 2010, A&A, 518, A10
Virtanen P. et al., 2020, Nat. Methods, 17, 261
Vogelsberger M. et al., 2014, Nature, 509, 177
Zakamska N. L., Greene J. E., 2014, MNRAS, 442, 784
Zubovas K., King A., 2012, ApJ, 745, L34

SUPPORTING INFORMATION

Supplementary data are available at *MNRAS* online.

Appendix A. Comments on individual galaxies.
Appendix B. Acquisition and spectrum.
Appendix C. Galaxy by galaxy data.
Appendix D. Gauss–Hermite higher order moments.
Appendix E. WHAN diagrams.

Please note: Oxford University Press is not responsible for the content or functionality of any supporting materials supplied by the authors. Any queries (other than missing material) should be directed to the corresponding author for the article.

This paper has been typeset from a TEX/LATEX file prepared by the author.

Downloaded from https://academic.oup.com/mnras/article/507/1/74/6324028 by Universidade Federal do Rio Grande do Sul user on 15 October 2021